Comparison of CERES-MODIS Stratus Cloud Properties with Ground-Based Measurements at the DOE ARM Southern Great Plains Site

Xiquan Dong[1], Patrick Minnis[2], Baike Xi[1], Sunny Sun-Mack[3], and Yan Chen[3]

[1] University of North Dakota, Grand Forks, ND

[2] NASA/Langley Research Center, Hampton, VA

[3] SAIC, Inc. Hampton, VA

Submitted to *Journal of Geophysical Research*, 19 January 2007

Corresponding author address: Dr. Xiquan Dong, The Department of Atmospheric Sciences, University of North Dakota, 4149 University Dr., Stop 9006, Grand Forks, ND 58202-9006. Email: dong@aero.und.edu. Phone: 701-777-6991.

Abstract

Global satellite data are critical for both verifying and improving GCM cloud parameterizations for climate prediction, but their utility is limited without a reasonable estimate of the errors in the satellite-derived cloud properties. As part of the continuing effort to estimate uncertainties in satellite-retrieved cloud properties, this paper compares overcast stratus cloud properties derived from MODIS on *Terra* and *Aqua* CERES project with observations taken at the DOE ARM SGP site from March 2000 to December 2004. The ARM surface data were averaged over a 1-hour interval centered at the time of each satellite overpass, and the CERES-MODIS cloud properties were averaged in a 30-km x 30-km box centered on the ARM SGP site. All cloud samples used in this study are overcast stratus with no overlying middle or high-level clouds. The effective cloud heights were derived using a lapse rate algorithm to convert the effective cloud temperature to height and are 0.59 $\pm$ 0.61 km less than the radar cloud tops and 0.15 $\pm$ 0.49 km less than the cloud centers with negligible day-night differences. During daytime, the CERES-derived cloud droplet effective radius r_e, optical depth τ, and liquid water path LWP values generally track the variations of the surface retrievals with a modest correlation in r_e and very high correlations in both τ and LWP. Differences between the *Terra* and surface retrievals are -2.8 $\pm$ 25%, -5.9 $\pm$ 27%, and -2.4 $\pm$ 31.5% for r_e, τ, and LWP, respectively. The corresponding differences for *Aqua* are 4.2 $\pm$ 25%, 6.8 $\pm$ 26%, and 25.2 $\pm$ 49.2%. Small calibration differences can account for the discrepancies in the mean r_e and τ differences for *Terra* and *Aqua*. The nighttime MODIS retrievals are, on average, consistent with the nighttime surface values and similar to their daytime counterparts, but there is no correlation between individual values.

1. Introduction

Clouds constitute one of the largest sources of uncertainty in predicting any potential future climate change [*Wielicki et al.,* 1995; *Houghton et al.,* 2001]. Thus, assessment of their interactions with the Earth's radiation budget and accurate representation of clouds in climate models have been classified as the highest priority by the U.S. Climate Change Research Initiative (USCCRI, 2001). The impact of clouds on the radiation budget mainly depends on cloud amount and height, cloud particle size and shape, and cloud (or ice) water content [e.g., *Curry et al.*, 2000; *Houghton et al.*, 2001]. This impact is highlighted by the wide range of cloud feedback results found in the *Cess et al.* [1990] intercomparison of 19 general circulation models (GCMs) that represented cloud microphysical and radiative processes in a variety of ways. The range of results narrowed as the cloud properties used in the models were altered [*Cess et al.,* 1996a]. Ultimately, the models should reproduce the cloud properties that are observed. Thus, global satellite data are critical for both verifying and improving GCM cloud parameterizations for climate prediction. Proper application of those data to climate questions requires a reasonable characterization of their uncertainties.

The NASA Clouds and the Earth's Radiant Energy System (CERES) project provides the first long-term global simultaneous measurements necessary for estimating the Earth's broadband radiation budget and retrieving cloud properties to achieve consistent radiative fluxes from the surface to the top of the atmosphere (TOA) [*Wielicki et al.,* 1998]. The CERES project was designed with specific climate accuracy goals for TOA, surface, and atmosphere fluxes matched with surface, cloud, and aerosol data [*Wielicki et al.,* 1995, 1996]. The CERES cloud and radiative flux data products should dramatically improve our understanding of cloud-radiation interactions, particularly, cloud feedback effects on the Earth radiation balance.

Therefore, the CERES data should be useful for studying climate system forcings and feedbacks to answer critical scientific questions and to understand and improve climate change simulations because they can be used to constrain GCMs. However, the limits placed on the GCM output can be no tighter than the accuracy of the observations.

Estimation of the errors in the derived cloud and radiative properties requires both theoretical evaluations of the measurement system capabilities and comparison with independent measurements of the same quantities. Ground-based measurements can provide independent "cloud-truth" data for estimating uncertainties in satellite-derived cloud properties, but they must first be properly analyzed and validated and their uncertainties must be understood. Comparisons between the ground- and satellite-based observations must be conducted carefully because of significant spatial and temporal differences between the two different observing platforms. Also because clouds are so variable, a statistically reliable validation requires coincident satellite-surface measurements taken in a variety of conditions. Complete validation of CERES cloud retrievals with independent ground-truth observations should account for the following variables: (1) cloud types (low, middle, high, multiple layer, and broken), (2) surface types (ocean, vegetated land, non-vegetated land, mountains, snow-covered land, and ice-covered water), (3) seasons, (4) day and night, and (5) viewing and illumination angles (e.g., satellite view zenith angle *VZA*, relative azimuth angle *RAA*, and solar zenith angle *SZA*). A complete quantitative assessment requires at least 100 independent samples for each of the conditions, and the independent samples must be typically 100-300 km apart and separated by 6 to 12 hours in time for clouds and radiation [*Wielicki et al.*, 2000]. Although the use of ground-based sensors, such as radar, lidar, and microwave radiometer, for validating satellite-derived cloud properties is well established [e.g., *Minnis et al.,* 1992, 1993; *Mace et al.,* 1998; *Greenwald et al.,* 1999; *Dong et*

al., 2001, 2002], reference or "cloud-truth" data are currently limited both geographically and temporally to a few types of clouds over particular areas, or limited to case studies. These case studies cannot provide a statistically reliable validation for different types of clouds in various climatic regimes. Therefore, complete validation of cloud retrievals in all conditions will take many years to achieve and will proceed in steps for particular conditions using the available reference datasets.

This paper presents a comparison of stratus cloud properties derived from Moderate Resolution Imaging Spectroradiometer (MODIS) data for CERES with ground-based observations from March 2000 to December 2004 at the Department of Energy Atmospheric Radiation Measurement (ARM) Program [*Ackerman and Stokes*, 2003] Southern Great Plains (SGP) site (36.6^{o}N, 262.5^{o}E). CERES single-layer cirrus cloud properties have been compared to radar and lidar-based observations in earlier studies [*Mace et al.,* 2005; *Chiriaco et al.,* 2007]. Here, low-level stratus cloud macrophysical and microphysical properties derived from the MODIS on *Terra* and *Aqua* as part of the CERES project are compared to simultaneous ground-based observations. The surface data are used as a “cloud truth” data set to validate the CERES-MODIS cloud properties and improve the CERES daytime and nighttime cloud retrieval algorithms. No attempt is made to exhaustively validate the CERES cloud retrieval algorithms; rather, our emphasis is to assess CERES-derived MODIS properties of both daytime and nighttime single-layer and overcast stratus clouds over the ARM SGP site. We focus this study on single-layer and overcast stratus clouds because the clouds are the closest to plane-parallel and are relatively well behaved with small uncertainties. Comparisons of stratus at other locations and of other types of clouds, such as cirrus, overlapped, and broken clouds, will be

undertaken as the surface retrieval algorithms are developed and verified by aircraft in situ measurements.

2. Data and Methods

Since there are significant spatial and temporal differences between surface and satellite observations, such as the relatively small sizes of the surface radar/lidar field-of-view as compared to the much larger satellite field-of-view, temporal and spatial scales should be matched as closely as possible during the surface-satellite comparison. The surface data were averaged over a 1-hour interval centered at the time of the satellite overpass, and the satellite data were averaged within a 30-km x 30-km area centered on the ARM SGP site. In a statistical context, the temporally averaged surface observations should be equivalent to the spatially averaged satellite results, as demonstrated by *Cess et al.* [1996b].

The ARM ground-based observations and retrievals, as well as their uncertainties and references used in this study, are listed in Table 1. The centerpiece of the cloud instrument array is the millimeter wavelength cloud radar [MMCR; *Moran et al.,* 1998]. The MMCR operates at a wavelength of 8 mm in a vertically pointing mode and provides continuous profiles of radar reflectivity from hydrometeors moving through the radar field of view, allowing the identification of clear and cloudy conditions. Cloud-top height (Z_{top}) is derived from cloud radar reflectivity profiles with an uncertainty of 45 m. Cloud-base height (Z_{base}) is derived from a composite of Belfort laser ceilometer, micropluse lidar, and cloud radar data [*Clothiaux et al.,* 2000]. For comparison with the satellite data, which are referenced to sea level, 0.317 km was added to each surface-determined cloud height. Cloud-base and -top temperatures, T_{base} and T_{top}, are estimated from a linear temporal interpolation of ARM SCF rawinsonde soundings (~4 times

per day) using Z_{base} and Z_{top}. The instantaneous soundings are first degraded to a common vertical resolution of 90 m before linear interpolation. The interpolated soundings, combined with other measurements, are denoted as ARM merged soundings. The cloud liquid water path (LWP) is derived from the microwave radiometer brightness temperatures measured at 23.8 and 31.4 GHz using a statistical retrieval method [*Liljegren et al.,* 2001].

To retrieve daytime microphysical properties of single-layer and overcast stratus clouds in the midlatitudes, *Dong et al.* [1997] used a δ2-stream radiative transfer model in conjunction with ground-based measurements. The retrieval scheme is based on an iterative approach that varies cloud-droplet effective radius (r_e) in the radiative transfer calculations until the model-calculated solar transmission matches the measured value. *Dong et al.* [1998] parameterized the retrieved r_e as a function of LWP, the solar transmission, and cos(SZA), μ_0. The optical depth τ is derived from the ratio of LWP and r_e. The nighttime r_e values are calculated from an empirical relationship between effective radius and radar reflectivity based on both theory and the daytime retrievals [*Dong and Mace*, 2003]. The retrieved and parameterized stratus cloud microphysical properties have been validated by in-situ aircraft measurements in the midlatitudes [*Dong et al.,* 1998 and 2002; *Dong and Mace*, 2003].

The satellite datasets used in this study are the *Terra* Edition2B and *Aqua* Edition1B 1-km pixel-level cloud properties that serve as input into the CERES Single Scanner Footprint (SSF) product. The SSF combines the CERES broadband flux measurements at a 20-km resolution with coincident, sub-sampled 1-km MODIS cloud and aerosol retrievals. The CERES cloud processing subsystem only analyzes every other pixel and every fourth scan line of the 1-km MODIS Collection-4 data. A set of algorithms and parameterizations [*Minnis et al.,* 1995, 1998, and 2004] were developed to derive cloud phase, effective cloud height (Z_e) and

161 temperature (T_e), r_e or ice-crystal effective diameter (D_e), τ, and *LWP* or ice water path (*IWP*) for
162 each imager pixel that is classified as cloudy by the CERES cloud mask. Six cloud masks were
163 developed to classify MODIS pixels for CERES as either cloudy or clear in non-polar [*Trepte et*
164 *al.,* 1999] and polar regions [*Trepte et al.,* 2002] during daytime ($SZA < 82^{\circ}$), twilight ($82° \leq SZA$
165 $\leq 88.5°$), and nighttime ($SZA > 88.5^{\circ}$). Each clear or cloudy pixel is further classified as "weak"
166 or "strong" to indicate the degree of confidence in each pixel's classification. These masks use
167 the 0.64 (VIS), 1.62, 3.78, 10.8 (IR), and 12.0-μm channels from MODIS. The primary
168 technique for determining Z_e is to first estimate T_e based on the IR radiance adjusted according to
169 τ, and then determine Z_e using either of two methods. For low clouds, a simple lapse rate
170 technique anchored to the surface temperature is used [*Minnis et al.,* 1992]. Over ocean and land
171 surfaces, the anchors are, respectively, the sea surface temperature and the running 24-h mean
172 surface temperature from the reanalyses provided by the Global Modeling Assimilation Office
173 GEOS 4.03 [*DAO*, 1997]. The surface-temperature anchored lapse rate of -7.1 K km^{-1} is blended
174 with the standard temperature profile from GEOS 4.03 between 700 and 500 hPa [*Minnis et al.,*
175 2003]. For higher clouds Z_e is defined as the lowest altitude having T_e in the GEOS vertical
176 profile of atmospheric temperature.

177 The main CERES daytime cloud microphysical retrieval algorithm is the 4-channel
178 VISST (Visible Infrared Solar-Infrared Split-window Technique), an updated version of the 3-
179 channel visible infrared solar-infrared method described by *Minnis et al.* [1995]. Given the
180 spectral clear-sky radiances and surface properties for a particular set of *SZA*, *VZA*, and *RAA*, the
181 VISST computes the spectral radiances expected at TOA for both water-droplet and ice-crystal
182 clouds over a range of optical depth from 0.25 to 128 for a particular cloud temperature. The
183 values of r_e for the model clouds range from 2 to 32 μm [*Minnis et al.,* 1998]. The modeled TOA

radiances include the attenuation of the radiation by the atmosphere and the impact of the radiation emitted or reflected by the surface. VISST relies on the IR radiance to determine T_e, the VIS reflectance to obtain τ, and the solar-infrared (SIR, 3.7 μm) radiance to estimate r_e. The split-window channel (SWC, 12.0 μm) is used to help determine phase. These parameters are determined iteratively for each pixel by matching the observed radiances to the modeled TOA radiances emittance and reflectance parameterizations that account for atmospheric attenuation and surface reflectance and emission [*Minnis et al.,* 1995 and 1998]. Cloud *LWP* is then deduced from the combination of the retrieved τ and r_e.

The nighttime CERES cloud microphysical retrieval algorithm, the Solar-infrared Infrared Split-window Technique [SIST; see *Minnis et al.,* 1995; *Heck et al.,* 1999], is used to retrieve cloud microphysical properties at night. The SIST utilizes the SIR, IR, and SWC channels simultaneously to determine cloud properties with a minimum-error, iterative regression method that matches the observations to parameterized model emittance calculations [*Minnis et al.,* 1995; *Smith et al.,* 1996]. To save computational time, thresholds are compared to the differences between the observed SIR and IR temperatures and between the IR and SWC temperatures to classify the pixel as optically thick or thin. If $\tau > 32$, the cloud is nominally assigned a default optical depth of 32 and default values of phase and particle size are assigned to the pixel. Two exceptions are used to apply a smaller default optical depth. If the observed IR temperature is 10 K colder than the predicted clear-sky value, the SIR-IR and IR-SWC brightness temperature differences are less than their corresponding predicted clear-sky values, and $\tau > 16$, then a default value of $\tau = 16$ is assigned to the cloud. If the IR temperature is greater than the predicted clear-sky value and $\tau > 8$, the default value of $\tau = 8$ is used. Otherwise, the SIST is applied, accepting results up to the default value. When the default optical depths are

used, the value of r_e is also set to a default value. Over land, if $\tau = 32$ or 16, then $r_e = 8$ μm. If $\tau = 8$, then $r_e = 6$. The corresponding values over ocean are 12 and 10 μm. The smaller value is selected because it is assumed that the cloud is a near-surface fog that results from abundant moisture and cloud condensation nuclei.

3. Results

An initial selection process based on the ARM radar-lidar observations identified a total of 109 *Terra* daytime and 49 nighttime single-layer and overcast stratus cases between March 2000 and December 2004. For *Aqua*, 69 daytime and 38 nighttime cases were identified in the same manner for data taken from July 2002 to December 2004 at the ARM SGP site. Examination of the satellite imagery was then used to further screen the data to remove scenes with overlying cirrus, broken cloud fields, or snow-covered surfaces. This process reduced the number of respective daytime and nighttime cases to 64 and 36 and to 45 and 33 for Terra and Aqua, respectively. Hereafter, *Terra* and *Aqua* refer to the CERES-MODIS retrievals from those satellites unless indicated otherwise.

3.1 Cloud height and temperature comparisons

Figure 1 shows time series (sample number is ordered from March 2000 through December 2004) of the *Terra* Z_e, T_e, and τ along with the surface-derived Z_{base}/Z_{top} and T_{base}/T_{top} for daytime single-layer and overcast stratus clouds at the ARM SGP site. These samples cover a wide range of cloud optical depths ranging from 2 to 128 (Figure 1c). In most instances, Z_e falls between Z_{top} and Z_{base} (Figure 1a). The corresponding values of T_e are 2 - 5 K less than their T_{top} counterparts for those same samples (Figure 1b). Overall, T_e tends to be a few Kelvins less than

T_{top} and does not exceed T_{basp}. Scatterplots of Z_e versus Z_{top} and Z_{mean} and of T_e versus T_{top} and T_{mean} are given in Figure 2. The parameters, Z_{mean} and T_{mean}, correspond to the altitude and temperature at the center of the cloud, respectively. Despite the relatively close tracking of the satellite and surface-derived heights in Figure 1a, the correlation coefficients only range between 0.39 and 0.50 (Figure 2a). The satellite and surface-derived cloud temperatures (Figure 2b) are much better correlated, ~0.95, than their height counterparts. The reduced correlation is in large part due to outlier samples 12, 21, 36, 39, and 62 where Z_e is significantly different from Z_{top}.

Table 2 summarizes the comparisons. The averaged T_e from *Terra* is nearly the same as the mean T_{top}, while the averaged Z_e is 0.53 km below Z_{top}, 0.08 km below Z_{mean}, and 0.37 km above Z_{base}. The standard deviations of the differences between Z_e and Z_{top}, Z_{mean}, and Z_{base} are 0.66, 0.50, and 0.51 km, respectively. The corresponding standard deviations (SD) in the temperature differences are 2.8, 2.6, and 3.2 K.

Time series of Z_e, T_e and τ from *Aqua* during July 2002 through December 2004 are shown in Figure 3 with the corresponding surface-derived values of Z_{base}/Z_{top} and T_{base}/T_{top} for daytime cases at the ARM SGP site. The scatters in those same data are plotted in Figure 4. The averaged *Aqua* T_e and Z_e are 1 K and 0.67 km less than T_{top} and Z_{top} (Figure 4), while the mean Z_e is 0.27 less than and 0.13 km greater than the average values of Z_{mean} and Z_{base}, respectively (Table 2, Figure 4a). Compared to the *Terra* results, fewer Z_e values are within the radar-lidar derived cloud boundaries and scatter around the cloud center (Figure 3a); more of them fall below cloud base. The correlation coefficients between the satellite and surface-determined temperatures (~0.9) in Table 2 are greater than those between Z_e and Z_{top}/Z_{mean} (~0.6). The SDs (Table 2) in the height and temperature differences are comparable to their *Terra* counterparts. The largest deviations from agreement in height (Figure 3a) occur for samples 5, 11, 13, and 44,

253 while the largest temperature differences (Figure 3b) occur for samples 3, 13, 33, and 42
254 including two cases with $T_e > T_{base}$.

255 Time series and scatterplots of nighttime cloud heights and temperatures are shown in
256 Figures 5 and 6 for *Terra* samples and in Figures 7 and 8 for the *Aqua* samples, respectively. As
257 demonstrated in the four figures and in Table 2, the nighttime satellite retrievals are similar to
258 their daytime counterparts relative to the MMCR observations. Most of the nighttime Z_e values
259 are below the radar-lidar derived cloud bases. The largest differences between Z_e and Z_{top} are for
260 *Terra* samples 5, 6, 14, and 29 (Figure 5). The largest differences for the *Aqua* data are for
261 samples 4, 12, 13, 14, and 23 (Figure 7). On average, Z_e is about halfway between the middle
262 and base of the clouds. As in the daytime cases, the averaged *Terra* and *Aqua* T_e values are
263 typically 1-2 K less than the mean T_{top} values and their correlations with T_{top}/T_{mean} are around
264 0.9. The correlations between Z_e and Z_{top}/Z_{mean} during nighttime (0.7-0.8) seen in Figures 6 and 8
265 are greater than those during daytime. These are reflected in the standard deviations of the
266 differences, which are slightly smaller than their daytime counterparts (Table 2). In all cases,
267 both day and night, the standard error in the mean differences between Z_e and Z_{mean} and between
268 T_e and T_{mean} are less than or equal to 0.11 km and roughly 0.5 K, respectively. Thus, these results
269 should be a good representation of the biases between the satellite and surface retrievals of
270 stratus cloud heights and temperatures.
271
272 ***3.2 Cloud microphysical property comparisons***
273 The number of cases used in the cloud microphysical property comparison is slightly
274 (e.g., 10 samples for *Terra*) less than that for the cloud height and temperature comparisons.
275 Samples were eliminated from microphysical comparisons if the data set lacked a key surface

measurement, such as solar transmission or *LWP,* or if the surface-derived *LWP* is too small (< 20 gm^{-2}) or too large (> 600 gm^{-2}) [*Dong et al.,* 1998]. Finally, some surface cloud cases have only height and temperature retrievals without microphysical retrievals because the clouds do not meet the retrieval criteria [*Dong et al.*, 1997].

The surface-retrieved cloud microphysical properties are compared with the matched daytime *Terra* and *Aqua* samples in Figures 9 - 12. The means and standard deviations of the differences between *Terra* and *Aqua* results relative to the surface retrievals are summarized in Table 3. In spite of the large differences in temporal and spatial resolution between surface and satellite, the time series of daytime VISST r_e, τ, and *LWP* values from both *Terra* and *Aqua* generally track the variations of the surface retrievals. The standard deviations in the satellite retrievals (not shown for sake of clarity) typically encompass the surface-derived values. The notable exceptions for r_e include samples 1, 18, 45, and 46 in Figure 9a and samples 7, 27, 30, 31, 35, 37, and 38 in Figure 11a. The apparently outstanding differences in τ are samples 11, 20, 45, and 47 in Figure 9b and samples 3, 27, and 38 in Figure 11b. The overall greater number of exceptions for r_e is reflected in the relatively modest correlation coefficients (Figures 10a and 12a, Table 3), while very high correlations are found in both τ and *LWP*. The *Terra* VISST optical depths and, hence, the *LWP* values at the low end tend to be smaller than those derived from the ARM instruments (Figures 10b-c), but are in better agreement for $\tau > 10$. For *Aqua*, the VISST yields greater values than from the surface for *LWP* > 200 gm^{-2} (Figure 12b-c). On average, the SDs in the r_e, τ, and *LWP* differences in the daytime VISST retrievals of r_e, τ, and *LWP* are 2.0 μm, 7.3, and 55 gm^{-2}, respectively. In relative terms, these SDs correspond to 25, 26, and 40%, respectively.

Similar comparisons for the nighttime stratus cloud microphysical properties are illustrated in Figures 13 - 16. These results are distinctly different from the daytime comparisons in that the satellite retrievals do not track their surface counterparts very well (Figures 13 and 15), especially the effective droplet size. The correlation coefficients for r_e are small negative values (Figures 14a and 16a, Table 3) indicating that the mixture of retrievals and defaults has no skill in measuring effective droplet radius. Minimal skill is found in the optical depth retrievals which yield small yet positive correlation coefficients for both satellites (Figures 14b and 16b), but it is lost in the *LWP* retrievals, which are highly scattered (Figures 14b and 16b). The standard deviations of the differences double the daytime values (Table 3). Remarkably, the mean differences are very close to their daytime counterparts and, in some cases, are actually smaller in magnitude. Thus, despite the lack of retrieval skill, the SIST manages to arrive at the proper mean value on average.

4. Discussion

4.1 Cloud heights

On average, the CERES-derived effective cloud heights are 0.59 and 0.17 km below the physical cloud top and center, respectively, observed by the MMCR. Since Z_e corresponds to the effective radiating temperature of the cloud, it is expected to be located at some point below the physical cloud top. *Cox and Griffith* [1979] assumed that the cloud liquid water content (*LWC*) was 1.0 gm^{-3} at the tops of low clouds and found that T_e would correspond to an altitude only 0.02 km below the top. For clouds with *LWC* = 0.1 and 0.05 gm^{-3}, that distance increases to 0.17 and 0.33 km, respectively, values closer to the present results. In situ observations and radar retrievals show a large variation in LWC within the top 0.30 km of stratus clouds. *Dong and*

Mace [2003] documented two stratus cases with $LWC \sim 0.1$ gm^{-3} near cloud top at the ARM SGP site and *Frisch et al.* [1998] reported a case with a mean value of ~0.09 gm^{-3} over the North Atlantic. In a review of in situ data, *Miles et al.* [2000] found ranges of 0.01 to 1.0 and 0.03 to 0.59 gm^{-3}, respectively, for continental and marine stratus and stratocumulus clouds. The mean in both cases is ~0.22 gm^{-3}. According to the *Cox and Griffith* [1979] calculations, this value would translate to a depth of only 0.09 km into the cloud top. Thus, only 15% of the mean Z_e - Z_{top} bias is likely to be explained by the radiating temperature effect. A correction for that effect is applied in the case of cirrus clouds to estimate Z_{top} from Z_e [*Minnis et al.*, 1995]. It is clear that a similar correction should be applied to the water-cloud heights also.

The remaining biases are due to conversion of T_e to altitude, residual cirrus contamination, and correction of the water vapor attenuation of the 11-μm channel. In the stratus cloud cases, the latter is typically small because the atmosphere above the single-layered stratus clouds is generally dry. Most cirrus-contaminated cases should have been eliminated in the secondary filtering of the datasets. Thus, the largest concern is translating T_e to a height. For a negative lapse rate, the lower values of T_e would indicate that Z_e should be higher than Z_{top}. However, the lapse rate technique used for the CERES retrieval is inherently different from the use of the ARM sounding to convert Z_{top} to T_{top}. Typically, satellite retrievals convert T_e to Z_e directly using a profile of T from a sounding or a numerical weather prediction (NWP) model analysis (e.g., *Rossow and Schiffer,* 1999), which is the inverse of the conversion of Z_{top} to T_{top}. If the sounding conversion approach were optimal, then T_e should be greater than or equal to T_{top}. Since $T_e < T_{top}$, on average, then T_{top} occurs too high in the sounding. *Garreaud et al.* [2001] found that rawinsondes often miss the coldest temperature under marine stratus inversions where cloud top occurs, likely as a result of the sharpness of the inversion and the relatively slow

thermal response of the instrument (e.g., *Mahesh et al.*, 1997). This overestimate of the minimum temperature below the inversion, even for the best sounding data possible, prompted the development of the lapse-rate approach to converting T_e to Z_e.

To determine whether Z_e would have been closer to Z_{top} if temperature profiles had been used, three experiments were conducted converting T_e to Z_e using the soundings from the ARM site. The first experiment degrades the merged ARM soundings to simulate the 25-hPa resolution of the GEOS profiles in the lower troposphere. To examine the impact of the resolution degradation, the second experiment employs the closest original high-resolution (25 - 40 m) ARM soundings that were taken within 3 hours of the satellite overpass. Typically those soundings were taken at 0530 or 1730 UTC. The third experiment uses the 6-hourly GEOS 4.03 profiles interpolated to the overpass time. For these experiments, the value of Z_e is determined by linear interpolation between Z_n and Z_{n-1} where n is the n^{th} level above the surface and $T(Z_n)$ is the first temperature in the profile above the surface where $T(Z_n) < T_e$. If the initial atmospheric temperature is less than T_e, then the height is set, as a default, to 0.5 km. This condition occurred very few times in the soundings.

Table 4 breaks down the experiment results for day and night and compares them to those from the lapse rate method. In both experiments using ARM soundings, Z_e overestimates Z_{top} by ~0.55 km compared to the underestimate of ~0.59 km by the lapse rate approach. In addition to reversing the sign of the bias, both experiments significantly increase the SD of the differences compared to those for the lapse-rate technique. Overall, the GEOS-like soundings increase the SDs by 72%. Surprisingly, the actual GEOS profiles yielded the smallest biases, ~0.37 km, overall. The accompanying difference SDs are comparable to those based on the ARM soundings. It is not clear why the GEOS 4.03 profiles yield results that are the same as, or

possibly even better than, the original soundings. Since the GEOS 4.03 includes the ARM soundings in its assimilation, it likely produces profiles comparable to the original soundings and performs a more realistic interpolation between them than the linear interpolation method used for the merged soundings. Fidelity of the GEOS 4.03 temperatures to those in the actual profiles over areas lacking nearby radiosonde soundings is likely to be less than at locations, such as the ARM site, where the input soundings are taken. A concomitant degradation in the resulting values of Z_e in those areas would also be expected. Considering all four datasets in Table 4, the magnitudes of the biases are not different at the 95% confidence level. Even if the 0.2 km reduction in the bias gained using the GEOS 4.03 temperature profile interpolation approach were significant, it would come at the cost of a dramatically increased instantaneous uncertainty.

Retrieving a low-cloud height with an accuracy better than $\pm$1 km is a difficult task, at least in the mid-latitudes and polar regions because of the complex structure of the lower troposphere. A reduction in the bias was the primary motivation for using the lapse rate technique over land for CERES Edition 2 processing. During the initial testing, the lapse rate used over ocean was applied and found to eliminate the bias over the SGP. Unfortunately, surface elevation was not taken into account when comparing the MMCR-derived and lapse-rate cloud-top heights. Furthermore, the lapse-rate tests (not published) were compared to results using temperature profiles from the European Center for Medium-Range Weather Forecasting (ECMWF) center that were employed for the CERES Terra Edition-1 processing [*Minnis et al.* 2002]. The ECMWF profiles yielded biases of 0.62 km in stratus cloud height, so the lapse rate approach was selected. Accounting for the 0.32-km surface height in the testing would have produced results similar to those found here and likely would have led to an adjustment of the lapse rate prior to the analyses. To minimize the bias over the SGP site, a lapse rate of -5 Kkm^{-1}

would need to be used. Its applicability to other regions besides the SGP needs further study. Nevertheless, the lapse rate approach significantly reduces the instantaneous error and, with future reductions in the bias, could provide a more accurate approach than using profiles from numerical weather analyses.

4.2 Microphysical properties

The good agreement between the surface and CERES-MODIS cloud microphysical properties and high level of correlation in cloud τ and LWP indicate that VISST can provide accurate and reliable retrievals of these parameters for overcast stratus clouds. The modest correlations in r_e and lack of a significant bias are puzzling, however.

4.2.1 Daytime cloud droplet sizes

Typically, the satellite-retrieved value of r_e (at 3.7 μm) is representative of cloud particle size near the cloud top for optically thick clouds [e.g., *Nakajima and King*, 1990]. The surface-retrieved layer-mean r_e represents the cloud particle size within the upper part of the cloud. In most instances, the droplet size increases with height in the cloud and r_e at the top should typically overestimate the value for the entire cloud. *Dong et al.* [2002] found that the VISST applied to a set of geostationary satellite data produced a 1.8-μm overestimate of r_e relative to the surface-derived values. One of the notable exceptions to that bias occurred when a thin layer overlaid the main deck of the clouds. In that case, the upper cloud had a smaller value of r_e than the lower cloud. The satellite-derived values were less than the surface retrievals because the satellite r_e retrieval corresponded mainly to the upper cloud. Perhaps, the occurrence of two layers is responsible for the lack of a bias in the VISST retrievals.

To test this hypothesis, the radar profiles for the *Aqua* cases were classified visually as having one or more layers in the stratus "deck". A system was defined as multilayered if it had more than one distinct separate layers or if it showed drizzle structure above and contiguous with an obvious lower layer. While the layering in most cases was relatively straightforward, several cases were ambiguous. Of the 44 cases, 21 were identified as multilayered while the remainder consisted of only one layer. The difference in r_e, i.e., r_e(CERES) – r_e(surface), was then matched with the layering for each case and used to determine the frequency of negative and positive differences for single and multilayered stratus cases. Positive differences were found for 87% of the single-layered cases and negative values occurred for 76% of the two-layer clouds. This simple analysis seems to confirm that much of the scatter and the lack of a bias are due to a nearly equal frequency of occurrence of single and multilayered stratus systems. Furthermore, the results suggest that, in most instances, the lower layer clouds are probably dominant in terms of mass and the upper layer clouds have smaller droplets, on average, than the lower layers. Additional analysis of this hypothesis is beyond the scope of this paper and is left for future research.

One means for addressing the ambiguity in the relationship between the actual and retrieved values of r_e is to make use of the other particle-size retrieval channels on MODIS. For example, *Chang and Li* [2003] showed that information about the vertical profile of r_e can be obtained from retrievals of r_e at 1.6, 2.1, and 3.7 μm. The shorter wavelengths yield values of r_e corresponding to thicker layers of the cloud top than for the 3.7-μm retrieval. Thus, for example, $r_e(1.6) > r_e(3.7)$ could indicate the presence of a thin layer over the bulk of the cloud deck. Multispectral retrievals of r_e are currently available from the MODIS standard atmospheric products [*Platnick et al.,* 2003] and will be part of future editions of the CERES products. Those

436 retrievals could be used along with the ARM radar-lidar retrieved vertical profiles of r_e [*Dong*
437 *and Mace*, 2003] to explore the multilayer hypothesis and other impacts of cloud vertical
438 structure on r_e retrievals.

439 The mean differences between r_e(CERES) and r_e(surface) are -0.22 and 0.34 μm for
440 *Terra* and *Aqua*, respectively. This 0.5-μm discrepancy between the *Terra* and *Aqua* retrievals is
441 seen in the global results and is due to the *Terra* 3.7-μm channel measuring brightness
442 temperatures that exceed their *Aqua* counterparts by ~0.5 K [*Minnis et al.*, 2006]. Based on this
443 calibration difference and the underestimation of r_e relative to the surface site, it is concluded
444 that the *Terra* values of r_e should be increased by ~0.5 μm or that future editions of the CERES
445 analysis use calibration-corrected *Terra* 3.7-μm radiances.

446

447 ***4.2.2 Daytime cloud optical depth and liquid water path***

448 Relative to the surface measurements, the optical depths retrieved from *Aqua* are 4.3 or
449 12.7% greater than those from *Terra* (Table 3). *Minnis et al.* [2007] found that the VIS channel
450 gain on *Aqua* is 1% greater than that on *Terra* prior to October 2003 and 2.1% greater thereafter.
451 This calibration difference will cause only negligible differences for $\tau < 10$, but would be
452 increasingly important at larger optical depths. For example, for $\tau = 32$ and $r_e = 8$ μm at *SZA* =
453 41°, the *Aqua* reflectance would yield optical depths of 34.3 and 37.1 compared to 32 for *Terra*
454 before and after October 2003, respectively. Accounting for the relative differences in calibration
455 before and after October 2003 for each case would reduce the mean *Aqua* optical depth by 1.7,
456 resulting in an average difference of 0.8 compared to the surface results. The adjusted mean
457 differences between the *Aqua* and *Terra* satellite-surface biases then would not be significant at
458 the 90% confidence level. Thus, it is concluded that the calibration differences between the two

satellite VIS channels could explain the relative differences seen in the satellite-surface comparisons. It is not clear which of the two channels has a more accurate absolute calibration.

When comparing the satellite and surface-based quantities, there is always some mismatch in terms of the actual portions of the clouds that are sampled. The time average of the clouds sampled by the small-beam radar and variable field-of-view (depends on cloud base height) is assumed to provide a value that is represented by the spatial average of the relatively large imager pixels. A more precise match of the data could have been attempted by using "wind-strips" of satellite pixels. Those strips of pixels correspond to the clouds advecting over the site during the averaging period of the surface instruments. As found by *Dong et al*. [2002], however, the more precise "strip" approach yields nearly the same statistics as the simple "box" average used here, presumably because there is no assurance that the relatively large pixels are represented by the beam averages on a one-to-one basis. Thus, the VISST values used here should be suitable for making the comparisons.

The SD of individual pixel values within the box provides a measure of the variability within the box and, therefore, the surface value plus its error should be within at least one SD from the satellite mean value. For *Aqua*, only two values of τ were outside of that bound (not shown), samples 5 and 22. In both instances, τ at the surface is around 10 and double the value from CERES), while r_e is the same from both perspectives. For both samples, the scenes appear to consist of a broken stratocumulus deck in the satellite imagery. For sample 5, taken at 2020 UTC, 25 October 2002, the cloud deck, although nearly overcast, rapidly moved and changed as evidenced by the imagery and analysis of the Eighth Geostationary Operational Environmental Satellite (GOES-8) data taken over the site (available at http://www-angler.larc.nasa.gov/satimage/products.html). Analyses of the GOES-8 data as in *Minnis et al.*

[2003] show that for a 40-km diameter circle around the SCF, τ changed from 4.1 to 8.4 to 16.8 at 1945, 2015, and 2045 UTC, respectively. A larger area average (100 km square box) of the MODIS pixels around the SCF yielded a $\tau = 8.5$, which is much closer to the surface-based value. Thus, much of the difference in that case may be attributed to broken structure and the changing nature of the cloud field that was not captured in the single MODIS image. The cloud field over the SCF was more broken during the sample-22 *Aqua* overpass at 1855 UTC, 6 October 2003. In this instance, many of the partially filled pixels were interpreted as overcast, so that the resulting optical depths were significantly reduced. This smearing effect operates whenever the clouds only fill part of the pixel. The radar could easily detect a line of cumulus clouds as being unbroken while the satellite "sees" clear pixels in the surrounding area.

Similar problems were encountered for the *Terra* comparisons. The optical depth differences that exceeded the value of τ from the VISST retrievals occurred for samples 3, 4, 11, 18, 20, 24, 45, and 47. The partially filled pixel cloud effect can explain the differences for samples 3-11, while a similar effect likely justifies the differences for samples 24 and 47. In the former case, a darker area is evident over the SCF. In the GOES analyses, the 20-km-diameter area yields a smaller average than the 40-km-diameter circle. Conversely, for sample 47 taken at 1730 UTC, 22 April 2004, the larger circle gives a smaller value of τ than the smaller circle. Another factor comes into play for some of the outliers. For example, both samples 18 and 24 were taken at high *VZA*s (63°) but the former viewed the clouds in the forward scattering hemisphere while the latter viewed at cross-scattering angles. Shadows from any cloud structure would tend to reduce the inferred optical depth when viewed in the forward direction at a high VZA, while the optical depth is enhanced in the cross-scattering view because of more side scatter by the cloud facets as found by *Loeb et al.* [1998] and *Chambers et al.* [2001]. Those

505 earlier studies also found that those types of differences become more pronounced with rising
506 SZA, so it is likely that the scatter would increase in results for areas with large SZAs. For
507 observations from a Sun-synchronous satellite like Terra, the departures from plane-parallel
508 behavior tend to average out over a period of time because the imager views from a different
509 perspective every overpass. For a geosynchronous satellite, this effect could produce a diurnal
510 bias since the satellite views from the same angles at a given hour each day. Correction for
511 impact of cloud structure and other systematic effects on the retrievals could be accomplished
512 either empirically or theoretically. However, the former would require a larger statistical
513 database than currently available and the latter would likely necessitate input of other variables,
514 such as cloud aspect ratio, that are not currently retrieved from passive imagery.

515 Because *LWP* is a product of τ and r_e, the *LWP* errors arise from errors in the other two
516 quantities. Thus, when either r_e or τ is under- or overestimated, *LWP* will follow. In some
517 instances, errors in either variable can cancel each other leading to a good estimate of *LWP* or
518 they can compound each other leading to extreme errors. This effect is highlighted in Figure 17,
519 which shows histograms of the satellite-surface differences for the three cloud microphysical
520 properties. In all three cases, ~53% of the differences are within 20% of zero. The center of the
521 *LWP* histogram is more peaked than the other two. Conversely, extreme *LWP* differences occur
522 more than twice as frequently as extreme r_e or τ differences.

523 Overall, the results are similar to those from *Dong et al.* [2002] except that r_e from GOES
524 was 1.8-µm larger than the surface retrieval and the *LWP* difference SD was smaller. For the
525 clouds sampled in the earlier study, the mean *LWP* was 89% larger than in the current analysis
526 and fewer two-layer systems were observed. This difference could explain the larger bias in the
527 GOES analysis. *Horvath and Davies* [2007] compared results from near-nadir MODIS standard

atmospheric products [*Platnick et al.,* 2003], MOD06, to *LWP* derived from a satellite-borne microwave imager over ocean and found that the differences were within 5-10% on average, with an instantaneous uncertainty of 35% for overcast boundary-layer clouds. Taking the *Terra* and *Aqua* results together, the mean *LWP* differences found here are similar to those from that study but the SD of the differences is larger by 4%. A smaller SD would be expected for the satellite-to-satellite comparison because the data were spatially matched and differ in time by no more than 15 minutes. The significant spatial differences and larger time differences in the surface-satellite comparisons drive up the SD in the comparison of those quantities. *Horvath and Davies* [2007] also found a slight increase in LWP with VZA, ~20% at VZA between 60 and 70°. Although the satellite-surface *LWP* difference increase with VZA is nearly identical, changing from 1% at VZA = 5° to 21% for *VZA* = 65°, there are too few samples to conclude that the trend is statistically significant.

4.3 Nighttime cases

Skill in retrieving cloud microphysical properties is not expected for many of these cases because the 11 and 12-μm signals are effectively lost when τ exceeds 5 or 6. The 3.7-μm channel still yields some information at larger optical depths, but it is not possible to separate optical depth and particle size effects on the signal without a second channel. The small mean differences in Table 3, therefore, are mostly serendipitous as a result of having appropriate default values. The SIST was primarily designed to account for the impact of the semi-transparency of optically thin clouds on the retrieved surface temperature. Although applied to all clouds with the aid of default values, the amount of information available for larger optical depths has not yet been researched systematically. With additional study of these channels

551 together with the MODIS 8.5-µm channel, it may be possible to extend the useful range of the
552 SIST and obtain better correlations than seen in Figures 14 and 16.
553
554 ***4.4 Discarded scenes***
555 In screening the original dataset, 33% of the cases identified as single-layered overcast
556 stratus were discarded because initial visual inspection of the satellite data revealed that the
557 scenes consisted of either broken or scattered clouds at the satellite pixel scale. Some of those
558 scenes were missed in the original screening as seen in the previous section. While the MMCR
559 indicated overcast directly over the site, it was missing gaps in the clouds due to favorable
560 alignment in the clouds or to a lack of advection in the cloud field. Some other cases containing
561 snow backgrounds were also eliminated because they require a different algorithm for satellite
562 analysis and introduce more errors in the surface retrievals of cloud microphysical properties.
563 Although those cases do not exactly fit the objective of this study, they can provide some insight
564 into quality of satellite retrievals in the less than ideal stratus cases that are often observed from
565 the satellite.
566 Adding the discarded 87 scenes to the results in Tables 2 and 3 increases the negative
567 bias in Z_e by 0.2 km in the daytime and by only 0.05 km at night relative to Z_{top}. The SD in the
568 Z_e- Z_{top} differences increases by 25% in all cases. The relative bias in T_e relative to T_{top} is close to
569 zero during the daytime when the non-overcast cases are included during the daytime. This effect
570 is probably the result of some clear-sky radiance affecting the satellite measurement in the
571 broken cloud fields. The change is smaller at night, most likely because the cloud-surface
572 temperature difference is substantially reduced from the daytime cases. The biases in r_e change
573 by less 3%, on average, during the day and approach zero at night, while SD(r_e) remains nearly

574 the same. The daytime biases in τ increase slightly during both day and night. No change is seen
575 in SD(τ) at night but it increases by 33% during the day. The overall impact on the *LWP*
576 comparisons is negligible. The rise in optical depth scatter during the day is expected because of
577 the increased three-dimensional structure in the broken clouds. Overall, it appears that the
578 inclusion of the clouds fields that are broken at the satellite scale mainly serves to increase the
579 scatter in the comparisons, but has minimal impact on the biases in the results.
580

581 **5. Conclusions**

582 Most of the daytime and nighttime CERES-MODIS-derived Z_e values are within the
583 radar-lidar derived cloud boundaries. The CERES-MODIS effective cloud heights correspond
584 most closely to the physical center of the cloud being, on average, 0.15 $\pm$ 0.49 km below it. The
585 value of Z_e underestimates the radar-derived cloud-top height by 0.59 $\pm$ 0.61 km. No significant
586 day-night difference was found in the analyses. The lapse rate approach to converting the
587 satellite-derived effective cloud temperature used for the CERES-MODIS retrievals yields a
588 slightly larger bias than the use of temperature profiles from radiosondes or NWP analyses.
589 However, the random error is substantially reduced with the lapse rate method instead of the use
590 of temperature profiles. Thus, adjustments in the lapse rate technique to reduce the bias error
591 should be effective in minimizing the overall error. Future versions of the CERES analyses will
592 include such adjustments.

593 The good agreement in the daytime cloud microphysical properties between the surface
594 and the CERES-MODIS retrievals and high correlations in cloud τ and *LWP* indicate that VISST
595 can provide accurate and reliable stratus cloud microphysical properties. The smaller correlation
596 in r_e appears to be primarily a result of layering within the stratus that alters the typical profile of

droplet size increasing from cloud bottom to top. Further study is needed to confirm this conclusion. However, with the ability to derive r_e simultaneously from shorter near-infrared wavelengths, it should be possible to estimate, at least, the sign of the vertical profile and improve the retrieval of r_e for many clouds. The 2.1-μm channel will be used for this purpose in future editions of CERES cloud products. Small discrepancies between the *Terra* and *Aqua* biases in r_e and τ appear to be due to uncorrected calibration differences. Although there seem to be some angular dependencies in some of the retrieved properties, especially *LWP*, there are not a sufficient number of samples available to make any firm conclusions about angular variations. With more samples, it might be possible to develop empirical correction methods to account for the plane-parallel model shortcomings in the current retrieval methods. The nighttime mean differences between surface and SIST results are small and nearly the same as daytime results, suggesting that the SIST retrievals are statistically consistent with the nighttime surface retrievals and close to their daytime counterparts. However, the relatively large standard deviations and small (even negative) correlations during nighttime indicate that the SIST needs further study and that the good agreement, on average, reflects the choice of default values in the analysis.

The results presented here represent only one class of clouds in a single area over a limited range of solar zenith angles. Without additional comparisons over other regions, it is not clear whether the current findings are representative of stratus clouds over land surfaces. More validation is needed for stratus clouds at different locations, such as polar, desert, and tropical regions, and also for different cloud types, including multilayered and broken clouds. Efforts are ongoing to address some of these other validation concerns, but the lack of fully instrumented surface sites in all climate regimes hampers this effort. Eventually, enough independent samples will be collected at the available sites to perform statistically significant surface-satellite

comparisons for several different climate regimes and cloud types. Angular and diurnal dependencies in the satellite retrievals can also be evaluated with additional samples and with comparisons to other satellites such as GOES. These limited site comparisons can be complemented on a global scale with new active sensors on satellites. With the 2006 launch of *CloudSat* and the Cloud-Aerosol Lidar and Infrared Pathfinder Satellite Observation satellite, it will be possible to perform similar comparisons globally from near-nadir views of *Aqua* MODIS thus giving the means to assess all cloud types over all regions at two local times and at one viewing zenith angle. Together with the surface measurements, these new data sources will provide the means to fully assess the errors in passive satellite cloud retrievals and the basis to make significant improvements in future editions of those retrieval algorithms.

Acknowledgments

The surface data were obtained from the Atmospheric Radiation Measurement (ARM) Program sponsored by the U.S. Department of Energy (DOE), Office of Energy Research, Office of Health and Environmental Research, Environmental Sciences Division. This research was supported by the NASA CERES project under grant NNL04AA11G at the University of North Dakota and by the ARM Program under interagency agreement DE-AI02-97ER62341.

643 REFERENCES

644 Ackerman, T. P., and G. M. Stokes (2003), The Atmospheric Radiation Measurement Program,
645 *Physics Today*, *56***,** 38-44.

646 Cess, R. D., and Coauthors (1990), Intercomparison and interpretation of climate feedback
647 processes in 19 atmospheric general circulation models, *J. Geophys. Res.*, *95*, 16,601-16,615.

648 Cess, B., and Coauthors (1996a), Cloud feedback in atmospheric general circulation models: An
649 update, *J. Geophys. Res.*, *101*, 12,791-12,794.

650 Cess, R. D., M. H. Zhang, Y. Zhou, X. Jing, and V. Dvortsov (1996b), Absorption of solar
651 radiation by clouds: Interpretations of satellite, surface, and aircraft measurements, *J.*
652 *Geophys. Res.*, *101*, 23,299-23,309.

653 Chambers, L. H., B. A. Wielicki, and N. G. Loeb (2001), Shortwave flux from satellite-measured
654 radiance: A theoretical study over marine boundary layer clouds, *J. Appl. Meteorol.*, *40*, 214-
655 2161.

656 Chang, F.-L., and Z. Li (2003), Retrieving vertical profiles of water-cloud droplet effective
657 radius: Algorithm modification and preliminary application, *J. Geophys. Res.*, *108*, D24,
658 4763, doi:10.1029/2003JD003906.

659 Chiriaco, M., and Coauthors (2007), Comparison of CALIPSO-like, LaRC, and MODIS
660 retrievals of ice cloud properties over SIRTA in France and Florida during CRYSTAL-
661 FACE, *J. Appl. Meteorol. Climatol.*, in press.

662 Clothiaux, E. E., T. P. Ackerman, G. G. Mace, K. P. Moran, R. T. Marchand, M. A. Miller, and
663 B. E. Martner (2000), Objective determination of cloud heights and radar reflectivities using
664 a combination of active remote sensors at the ARM CART sites, *J. Appl. Meteorol., 39*, 645-
665 665.

666 Cox, S. K., and K. T. Griffith (1979), Estimates of radiative divergence during Phase III of the
667 GARP Atlantic Tropical Experiemnt: Part I. Methodology, *J. Atmos. Sci.*, **36**, 576-585.
668 Curry, J.A., and Coauthors (2000), FIRE Arctic Clouds Experiment. *Bull. Am. Meteorol. Soc.*,
669 *81*, 5-29.
670 DAO (1997), GEOS-3 Data Assimilation System Architectural Design, *DAO Office Note 97-06*,
671 Data Assimilation Office, Goddard Space Flight Center, Greenbelt, MD 20771.
672 Dong, X., T. P. Ackerman, E. E. Clothiaux, P. Pilewskie, and Y. Han (1997), Microphysical and
673 radiative properties of stratiform clouds deduced from ground-based measurements. *J.*
674 *Geophys. Res.*, *102*, 23,829-23,843.
675 Dong, X., T. P. Ackerman, and E. E. Clothiaux (1998), Parameterizations of microphysical and
676 shortwave radiative properties of boundary layer stratus from ground-based measurements.
677 *J. Geophys. Res.*, *103*, 31,681-31,693.
678 Dong, X., G. G. Mace, P. Minnis, and D. F. Young (2001), Arctic stratus cloud properties and
679 their effect on the surface radiation budget: Selected cases from FIRE ACE, *J. Geophy. Res.*
680 *106*, 15,297-15,312.
681 Dong, X., P. Minnis, G. G. Mace, W. L. Smith Jr, M. Poellot, R. Marchand, and A. Rapp (2002),
682 Comparison of stratus cloud properties deduced from surface, GOES, and aircraft data during
683 the March 2000 ARM Cloud IOP, *J. Atmos. Sci., 59*, 3265-3284.
684 Dong, X. and G. G. Mace (2003), Profiles of low-level stratus cloud microphysics deduced from
685 ground-based measurements, *J. Atmos. and Oceanic Tech., 20*, 42-53.
686 Garreaud, R. D., J. Rutllant, J. Quintana, J. Carrasco, and P. Minnis (2001), CIMAR-5: A
687 snapshot of the lower troposphere over the subtropical southeast Pacific, *Bull. Amer. Meteor.*
688 *Soc.*, **92**, 2193-2208.

689 Greenwald, T. J., S. A. Christopher, J. Chou, and J. C. Liljegren (1999), Intercomparison of
690 cloud liquid water path derived from the GOES-9 imager and ground-based microwave
691 radiometers for continental stratus, *J. Geophys. Res., 104,* 9521-9260.
692 Heck, P. W., W. L. Smith, Jr., P. Minnis, and D. F. Young (1999), Multispectral retrieval of
693 nighttime cloud properties for CERES, ARM, and FIRE, *Proc. of the ALPS 99 Conference*,
694 Meribel, France, January 18-22, WK-P-03,1,4. [Available at http://www-pm.larc.nasa.gov/
695 ceres/pub/conference/Heck.ALPS_99.pdf]
696 Horváth, Á., and R. Davies (2007), Comparison of microwave and optical cloud water path
697 estimates from TMI, MODIS, and MISR, *J. Geophys. Res.*, *112*, D01202,
698 doi:10.1029/2006JD007101.
699 Houngton, J. T., and coauthors (2001), *Climate Change 2001: The Scientific Basis,* Cambridge
700 University Press.
701 Liljegren, J. C., E. E. Clothiaux, G. G. Mace, S. Kato, and X. Dong (2001), A new retrieval for
702 cloud liquid water path using a ground-based microwave radiometer and measurements of
703 cloud temperature, *J. Geophys. Res.*, *106*, 14,485-14,500.
704 Loeb, N. G, T. Varnai, and D.M. Winker (1998), Influence of subpixel-scale cloud-top structure
705 on reflectances from overcast stratiform cloud layers, *J. Atmos. Sci.*, *55*, 2960-2973.
706 Mace, G. G., T. P. Ackerman, P. Minnis, and D. F. Young (1998), Cirrus layer microphysical
707 properties derived from surface-based millimeter radar and infrared interferometer data. *J.*
708 *Geophys. Res.*, *103*, 23,207-23,216.
709 Mace, G. G., Y. Zhang, S. Platnick, M. D. King, P. Minnis, and P. Yang (2005), Evaluation of
710 cirrus cloud properties from MODIS radiances using cloud properties derived from ground-
711 based data collected at the ARM SGP site, *J. Appl. Meteorol., 44*, 221-240.

712 Mahesh, A., V. P. Walden, and S. G. Warren (1997), Radiosonde temperature measurements in
713 strong inversions: Correction for thermal lag based on an experiment at the South Pole, *J.*
714 *Atmos. Oceanic Technol.*, *14*, 45-53.
715 Miles, N. L., J. Verlinde, and E. E. Clothiaux (2000), Cloud droplet distributions in low-level
716 stratiform clouds, *J. Atmos. Sci.*, **57**, 295-311.
717 Minnis, P., D. R. Doelling, L. Nguyen, and W. F. Miller (2007), Assessment of the visible
718 channel calibrations of TRMM VIRS and MODIS on Aqua and Terra, *J. Atmos. Oceanic*
719 *Technol.*, submitted.
720 Minnis, P., and Coauthors (2006), Overview of CERES cloud properties from VIRS and
721 MODIS, *Proc. AMS 12th Conf. Atmos. Radiation*, Madison, WI, July 10-14, CD-ROM, J2.3.
722 Minnis, P., P. W. Heck, and D. F. Young (1993), Inference of cirrus cloud properties using
723 satellite-observed visible and infrared radiances, Part II: Verification of theoretical cirrus
724 radiative properties, *J. Atmos. Sci.*, *50*, 1305-1322.
725 Minnis, P., P. W. Heck, D. F. Young, C. W. Fairall, and J. B. Snider (1992), Stratocumulus cloud
726 properties derived from simultaneous satellite and island-based instrumentation during FIRE,
727 *J. Appl. Meteorol.*, *31*, 317-339.
728 Minnis, P., and Coauthors (1995), Cloud Optical Property Retrieval (Subsystem 4.3). Clouds
729 and the Earth's Radiant Energy System (CERES) Algorithm Theoretical Basis Document,
730 Volume III: Cloud Analyses and Radiance Inversions (Subsystem 4), *NASA Tech. Rep. RP*
731 *1376,* 135-176.
732 Minnis, P., D. P. Garber, D. F. Young, R. F. Arduini, and Y. Takano (1998), Parameterization of
733 reflectance and effective emittance for satellite remote sensing of cloud properties. *J. Atmos.*
734 *Sci.*, *55*, 3313-3339.

735 Minnis, P., W. L. Smith, Jr., L. Nguyen, J. J. Murray, P. W. Heck, and M. M. Khaiyer (2003),
736 Near-real-time satellite cloud products for icing detection and aviation weather over the
737 USA, *Proc. FAA In-Flight Icing/De-icing Intl. Conf.*, Chicago, IL, June 16-20, CD_ROM,
738 2003-01-2097.
739 Minnis, P., and Coauthors (2002), A global cloud database from VIRS and MODIS for CERES.
740 *Proc. SPIE Conf. Optical Remote Sens. Of Atmosphere and Clouds III*, Hangzhou, China.
741 Mitchell, J. F. B. and W. J. Ingram (1992), Carbon dioxide and climate: Mechanisms of changes
742 in cloud, *J. Climate, 5,* 5-21.
743 Moran, K. P., B. E. Martner, M. J. Post, R. A. Kropfli, D. C. Welsh, and K. B. Widener (1998),
744 An unattended cloud-profiling radar for use in climate research, *Bull. Am. Meteorol. Soc*., *79*,
745 443-455.
746 Nakajima, T. and M. D. King (1990), Determination of the optical thickness and effective
747 particle radius of clouds from reflected solar radiation measurements. Part I: Theory, *J.*
748 *Atmos. Sci.*, *47*, 1878-1893.
749 Platnick, S., M. D. King, S. A. Ackerman, W. P. Menzel, B. A. Baum, J. C. Ridi, and R. A
750 Frey,(2003), The MODIS cloud products: Algorithms and examples from Terra, *IEEE Trans.*
751 *Geosici. Remote Sens.*, *41*, 459-473.
752 Rossow, W. B. and R. A. Schiffer (1999) Advances in understanding clouds from ISCCP, *Bull.*
753 *Amer. Meteor. Soc.*, *80*, 2261-2287.
754 Smith, W. L., Jr., L. Nguyen, D. P. Garber, D. F. Young, P. Minnis, and J. Spinhirne (1996),
755 Comparisons of cloud heights derived from satellite and ARM surface lidar data, *Proc. 6th*
756 *Annual ARM Science Team Meeting*, San Antonio, TX, Mar. 4-7, 287-291. [Available at
757 http://www.arm.gov/publications/proceedings/conf06/extended_abs/smith_wl.pdf]

758 Trepte, Q., Y. Chen, S. Sun-Mack, P. Minnis, D. F. Young, B. A. Baum, and P. W. Heck (1999),
759 Scene identification for the CERES cloud analysis subsystem, *Proc. AMS 10th Conf. Atmos.*
760 *Rad.*, Madison, WI, June 28 – July 2, 169-172.
761 Trepte, Q., P. Minnis, and R. F. Arduini (2002), Daytime and nighttime polar cloud and snow
762 identification using MODIS data, *Proc. SPIE 3rd Intl. Asia-Pacific Environ. Remote Sensing*
763 *Symp. 2002: Remote Sens. of Atmosphere, Ocean, Environment, and Space*, Hangzhou,
764 China, October 23-27, Vol. 4891, 449-459.
765 Turner, D. D., and Coauthors (2007), Optically thin liquid water clouds: Their importance and
766 our challenge, *Bull. Am. Meteorol. Soc.*, in press.
767 Wielicki, B.A., R.D. Cess, M.D. King, D.A. Randall, and E.F. Harrison (1995), Mission to planet
768 Earth: Role of clouds and radiation in climate. *Bull. Am. Meteorol. Soc.*, *76*, 2125-2153.
769 Wielicki, B. A, B. R. Barkstorm, E. F. Harrison, R. B. Lee III, G. L. Smith, and J. E. Cooper
770 (1996), Clouds and the Earth's Radiant Energy System (CERES): An Earth Observing
771 System Experiment, *Bull. Am. Meteorol. Soc.*, *77*, 853-868.
772 Wielicki, B.A. and Co-authors (1998), Clouds and the Earth's Radiant Energy System (CERES):
773 Algorithm overview, *IEEE Trans. Geosci. Remote Sens., 36*, 1127-1141.
774 Wielicki, B. A. and Co-authors (2000), CERES Validation Plan Overview, Release 4, 10/20/00,
775 58 pp. (Available at http://asd-www.larc.nasa.gov/ceres/validation/ceresval_r4.0_over.pdf)
776

Figure captions

Figure 1. Time series of surface-derived cloud-base and -top heights and temperatures (1-hour average) and matched *Terra* MODIS-derived effective cloud heights and temperatures (30-km x 30-km average) for daytime single-layer, overcast stratus clouds over the ARM SGP site (sample number is ordered from March 2000 to December 2004).

Figure 2. Same as Fig. 1, except for scatterplots.

Figure 3. Same as Figure 1, except for matched daytime *Aqua* data (sample number is ordered from July 2002 to December 2004).

Figure 4. Same as Fig. 3, except for scatterplots.

Figure 5. Same as Fig. 1, except for nighttime results.

Figure 6. Same as Fig. 5, except for scatterplots.

Figure 7. Same as Fig. 3, except for nighttime results.

Figure 8. Same as Fig. 7, except for scatterplots.

Figure 9. Time series of surface-derived (1-hour average) and matched CERES *Terra* MODIS-derived cloud parameters (30-km x 30-km average), a) cloud-droplet effective radius, b) optical depth, and c) LWP, for daytime single-layer, overcast stratus clouds over the ARM SGP site (sample number is ordered from March 2000 to December 2004). Error bars denote SD of CERES parameters.

Figure 10. Scatterplots of data presented in Figure 9.

Figure 11. Same as Figure 9, except for *Aqua* (sample number is ordered from July 2002 to December 2004).

Figure 12. Same as Figure 10, except data from Figure 11 (daytime *Aqua*-surface retrievals) are plotted.

Figure 13. Same as Fig. 9, except for *Terra* nighttime results.

Figure 14. Same as Figure 10, except results from Figure 13 (nighttime *Terra*-surface retrievals) are plotted.

Figure 15. Same as Fig. 9, except for *Aqua* nighttime results.

Figure 16. Same as Fig. 10, except for *Aqua* nighttime results.

Figure 17. Histograms of daytime cloud property differences between CERES MODIS and surface-based retrievals from data presented in Figures 10 and 12.

Table captions

Table 1. Surface-derived cloud properties and their uncertainties.

Table 2. Means and standard deviations (SD) of differences and linear correlation coefficients (Corr) of CERES MODIS-retrieved effective cloud height and temperature relative to surface-observed cloud height and temperature.

Table 3. Means and standard deviations (SD) of differences and linear correlation coefficients (Corr) of MODIS retrievals relative to surface results.

Table 4. Comparison of cloud height differences using different temperature-to-height conversion techniques using *Aqua* and *Terra* data as in Table 2.

832 Table 1. Surface-derived cloud properties and their uncertainties

Cloud Property	Uncertainty	Instrument and retrieval algorithm
Cloud-base height	8 m	Laser ceilometer or lidar
Cloud-top height	45 m	Microwave cloud radar (MMCR)
Cloud-base/-top temp	0.2^{o} C	Vaisala radiosonde
Cloud-droplet effective radius	~ 10 % for day ~ 15% for night	Dong et al., 1997, 1998, 2002 Dong and Mace, 2003
Cloud optical depth	~ 5% for day ~ 5-10% for night	Dong et al., 1997, 1998, 2002 Dong and Mace, 2003
Cloud LWP	20 gm^{-2} < LWP < 200 gm^{-2}, 20 gm^{-2} LWP > 200 gm^{-2}, ~10%	LWP retrieved from microwave radiometer measured brightness temp. Dong et al., 2000; Liljegren et al., 2001

833

834

835

836

Table 2. Means and standard deviations (SD) of differences and linear correlation coefficients (Corr) of CERES MODIS-retrieved effective cloud height and temperature relative to surface-observed cloud height and temperature.

	Number of Samples	$Z_e - Z_{base}$			$Z_e - Z_{mean}$			$Z_e - Z_{top}$		
		Mean (km)	SD (km)	Corr	Mean (km)	SD (km)	Corr	Mean (km)	SD (km)	Corr
Terra, day	64	0.369	0.509	0.436	-0.082	0.495	0.50	-0.534	0.655	0.394
Aqua, day	45	0.125	0.557	0.567	-0.274	0.512	0.651	-0.673	0.597	0.608
Terra, night	36	0.060	0.468	0.825	-0.309	0.487	0.803	-0.678	0.637	0.70
Aqua, night	33	0.320	0.564	0.694	-0.075	0.42	0.827	-0.471	0.481	0.80
		$T_e - T_{base}$			$T_e - T_{mean}$			$T_e - T_{top}$		
		Mean (K)	SD (K)	Corr	Mean (K)	SD (K)	Corr	Mean (K)	SD (K)	Corr
Terra, day	64	-2.95	3.15	0.924	-2.37	2.55	0.955	-1.77	2.81	0.943
Aqua, day	45	-2.26	2.95	0.916	-1.63	2.89	0.92	-1.02	3.52	0.877
Terra, night	36	-2.46	3.02	0.93	-2.31	2.44	0.952	-1.797	3.07	0.923
Aqua, night	33	-3.61	4.8	0.753	-3.1	2.91	0.896	-2.61	2.54	0.922

Table 3. Means and standard deviations (SD) of differences and linear correlation coefficients (Corr) of MODIS retrievals relative to surface results.

	Number of samples	r_e*(CERES)*-r_e*(sfc)*			τ*(CERES)*-τ*(sfc)*			LWP*(CERES)*-LWP*(sfc)*		
		Mean (μm)	SD (μm)	Corr	Mean	SD	Corr	Mean (gm^{-2})	SD (gm^{-2})	Corr
Terra, day	54	-0.22	1.98	0.44	-1.72	7.92	0.91	-3.61	46.72	0.91
Aqua, day	44	0.34	1.99	0.39	2.55	6.58	0.96	32.68	63.77	0.91
Terra, night	24	-1.04	3.47	-0.12	-0.09	12.1	0.04	-0.29	86.06	-0.26
Aqua, night	30	-1.08	3.79	-0.09	-2.39	10.2	0.27	-12.3	92.2	0.04
		r_e*(CERES)*-r_e*(sfc)*		τ*(CERES)*-τ*(sfc)*		LWP*(CERES)*-LWP*(sfc)*	
		Mean (%)	SD (%)	Mean (%)	SD (%)	Mean (%)	SD (%)
Terra, day	54	-2.8	24.8	-5.9	27.0	-2.4	31.5
Aqua, day	44	4.2	24.8	6.8	26.0	25.2	49.2
Terra, night	24	-11.2	37.4	-0.5	69.8	-0.3	88.8
Aqua, night	30	-11.6	40.8	-12.8	54.8	-11.0	82.7

Table 4. Comparison of cloud height differences using different temperature-to-height conversion techniques using *Aqua* and *Terra* data as in Table 2.

Method	Samples	Z_{top} (km)	Z_e - Z_{top} (km)	$SD(Z_e - Z_{top})$ (km)
Lapse rate (day)	109	1.91	-0.591	0.631
Merged sounding (day)	109	1.91	0.54	1.088
ARM sounding (day)	68	2.31	0.498	1.104
GEOS 4.03 (day)	109	1.91	0.378	1.086
Lapse rate (night)	69	2.01	-0.579	0.588
Merged sounding (night)	69	2.01	0.57	0.963
ARM sounding (night)	39	2.38	0.609	0.808
GEOS 4.03	69	2.01	0.368	1.014

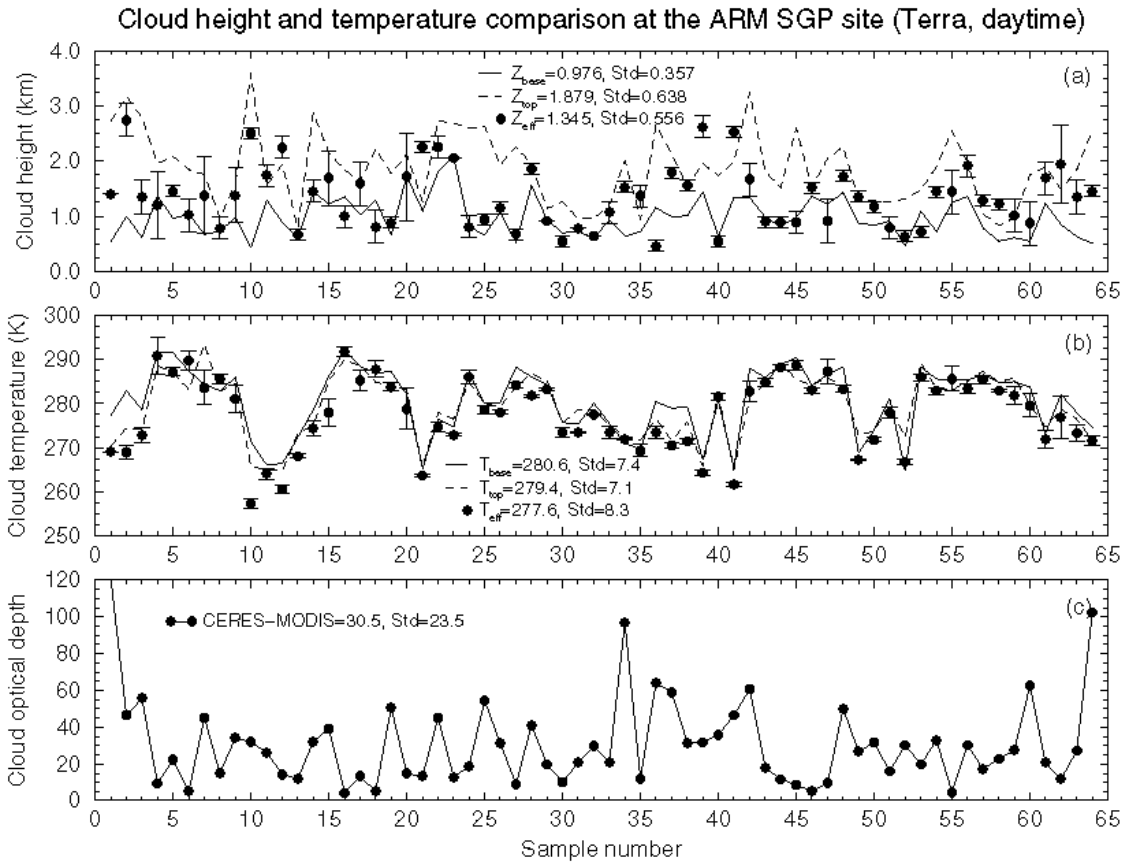

860

861 Figure 1. Time series of surface-derived cloud-base and -top heights and temperatures (1-hour
862 average) and matched *Terra* MODIS-derived effective cloud heights and temperatures (30-km x
863 30-km average) for daytime single-layer, overcast stratus clouds over the ARM SGP site (sample
864 number is ordered from March 2000 to December 2004).
865

866

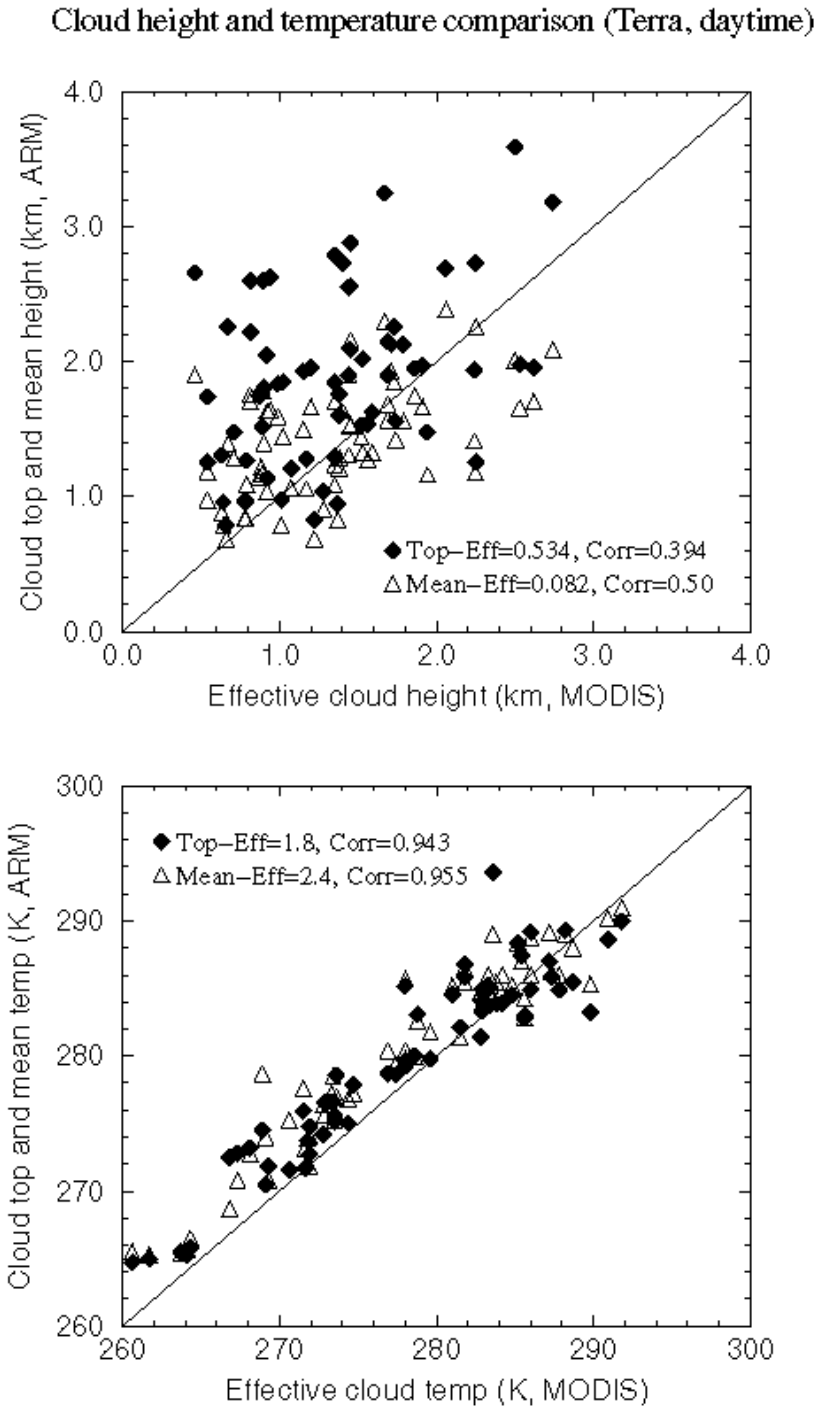

867

868 Figure 2. Same as Fig. 1, except for scatterplots.

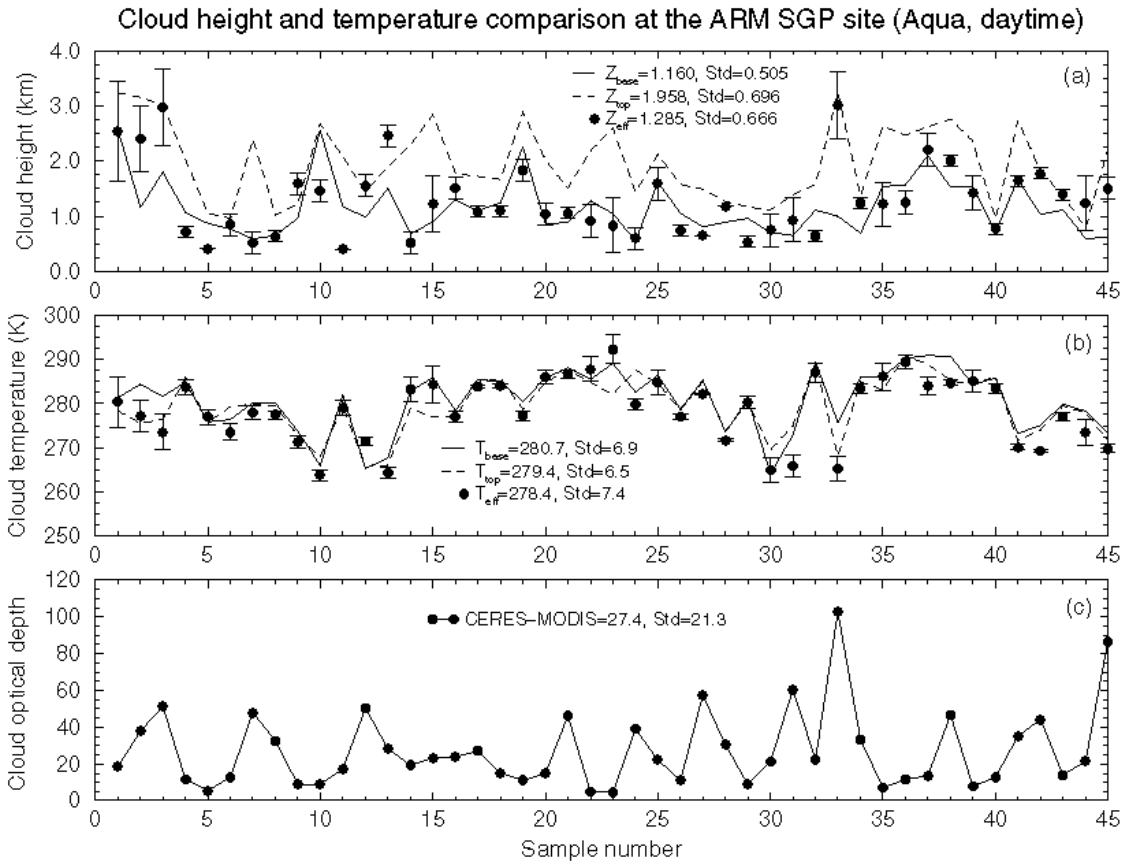

869

870 Figure 3. Same as Figure 1, except for matched daytime *Aqua* data (sample number is ordered
871 from July 2002 to December 2004).
872

873

874

875

876

877

878

879

880

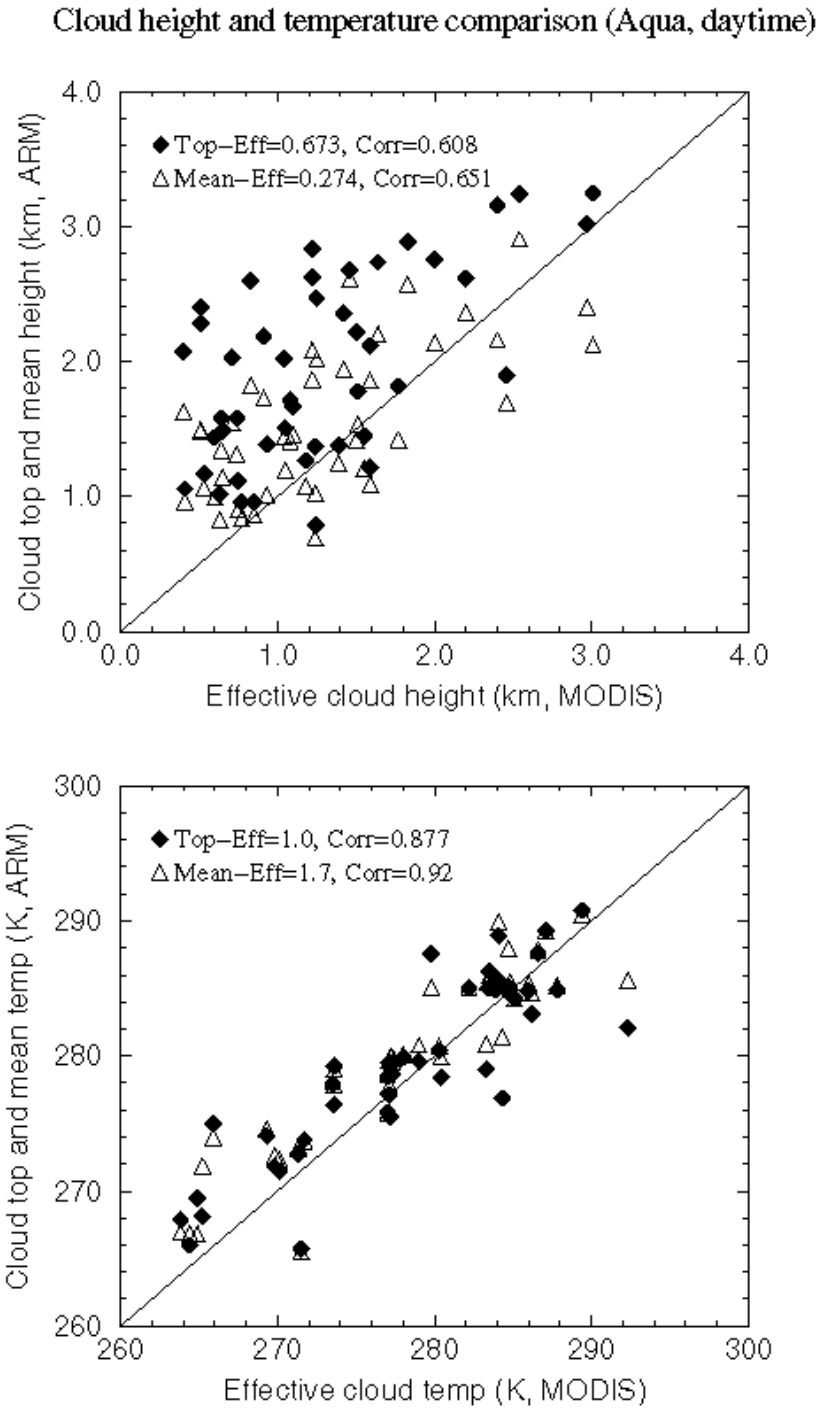

881

882 Figure 4. Same as Fig. 3, except for scatterplots.

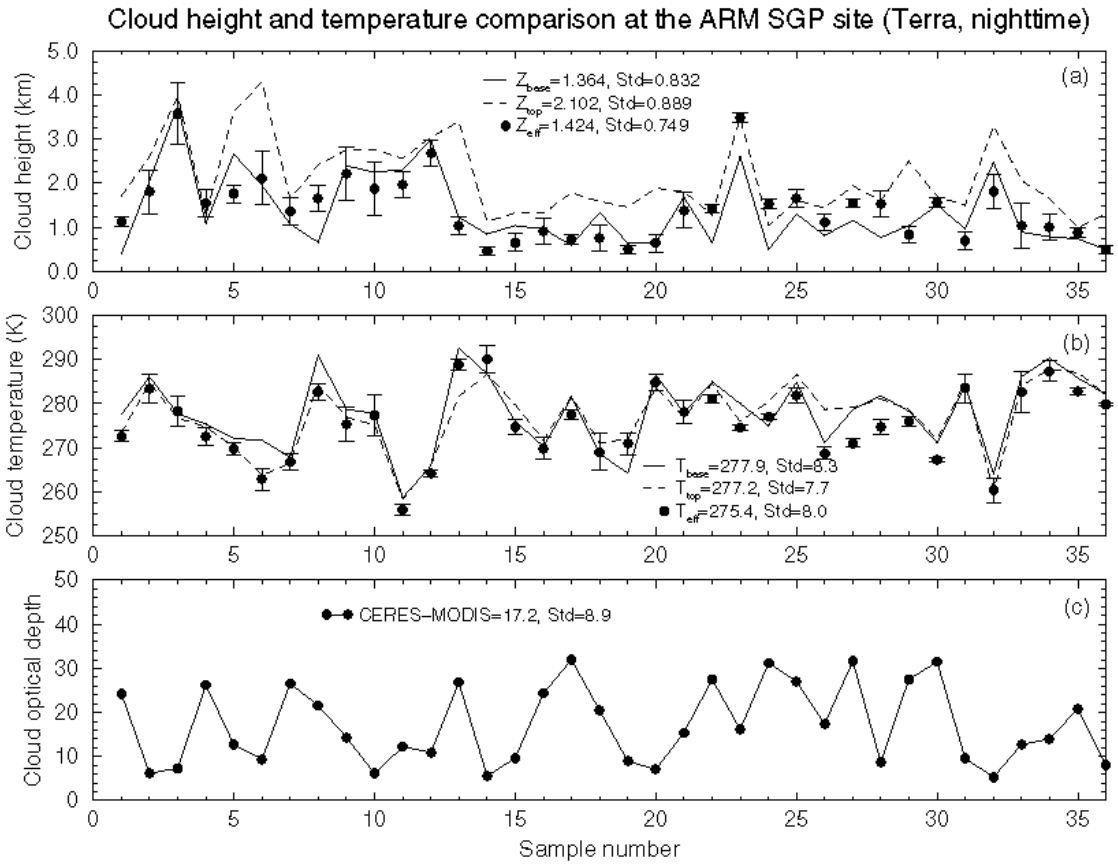

883

884 Figure 5. Same as Fig. 1, except for nighttime results.

885

886

887

888

889

890

891

892

893

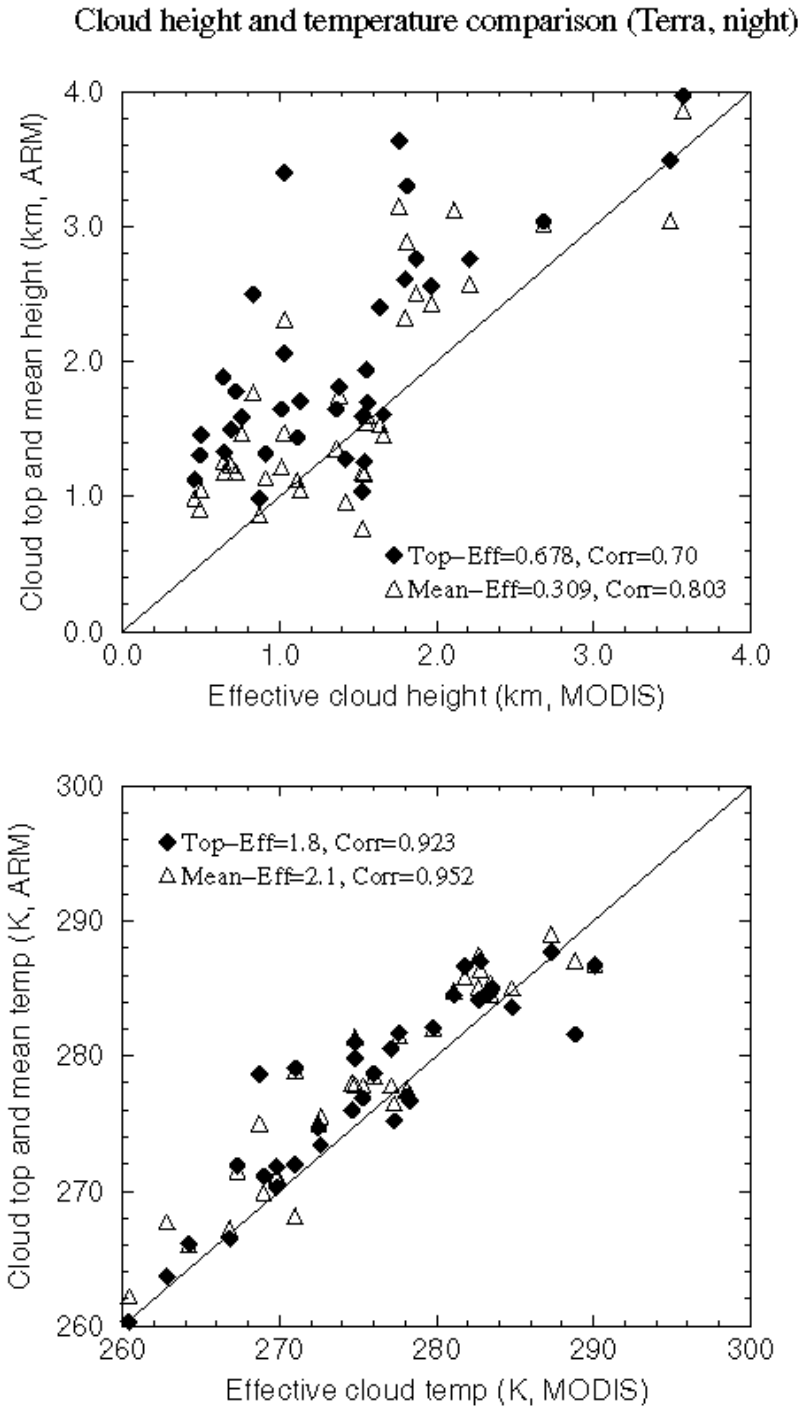

894

895 Figure 6. Same as Fig. 5, except for scatterplots.

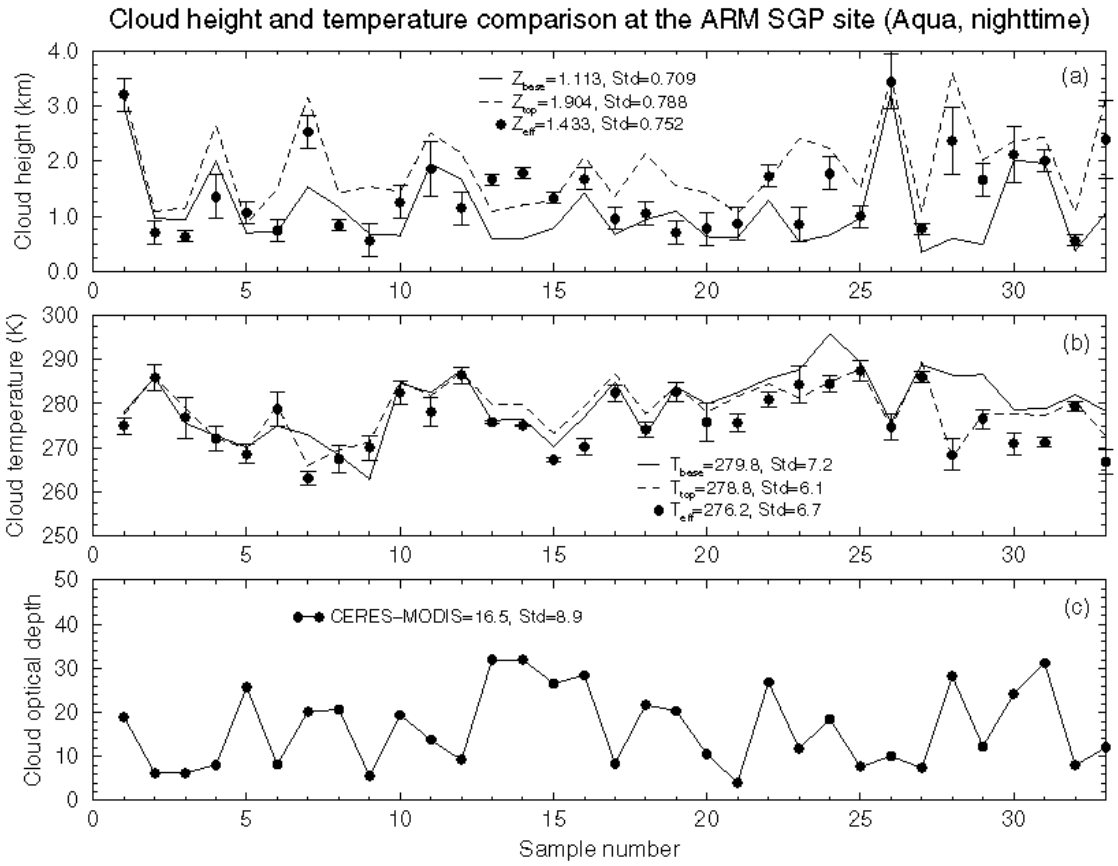

Figure 7. Same as Fig. 3, except for nighttime results.

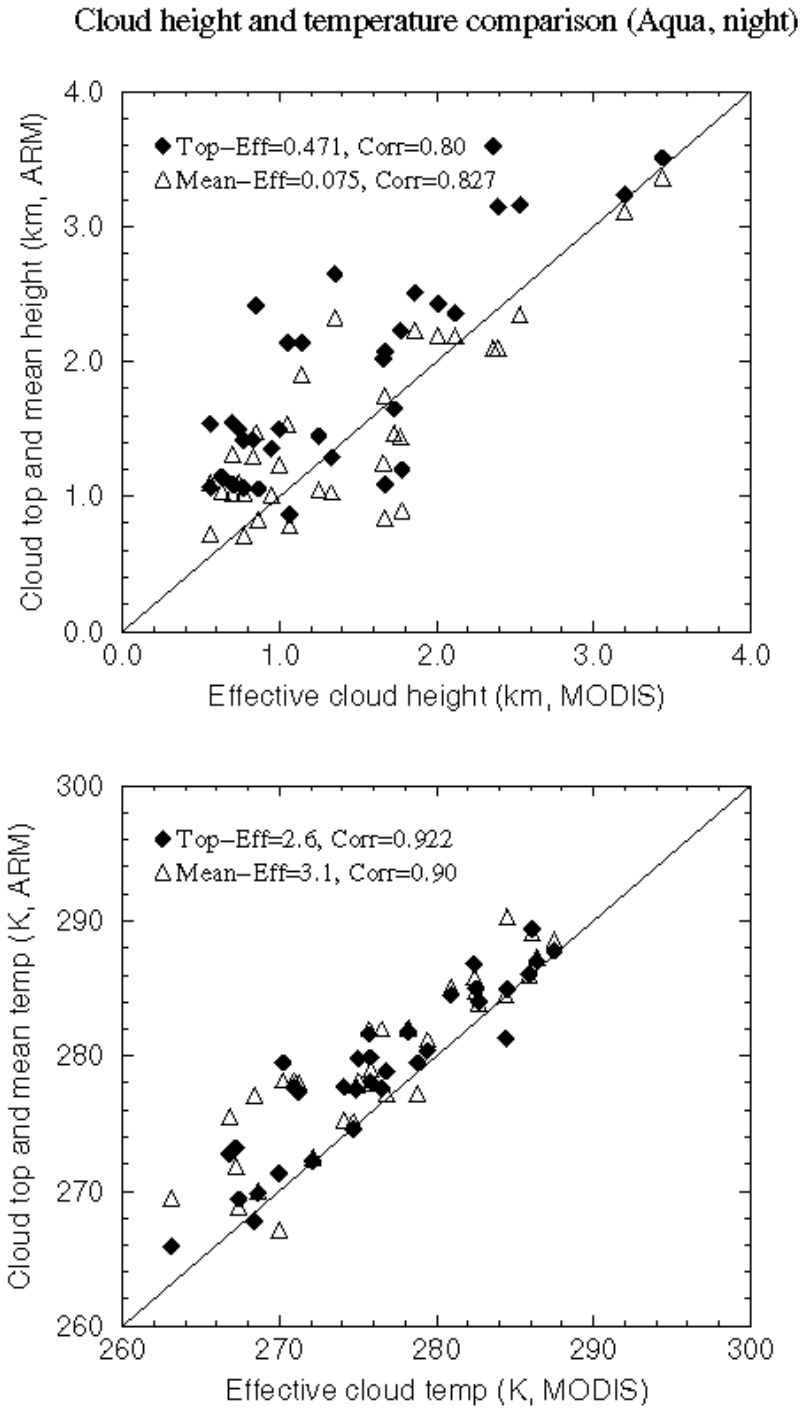

907

908 Figure 8. Same as Fig. 7, except for scatterplots.

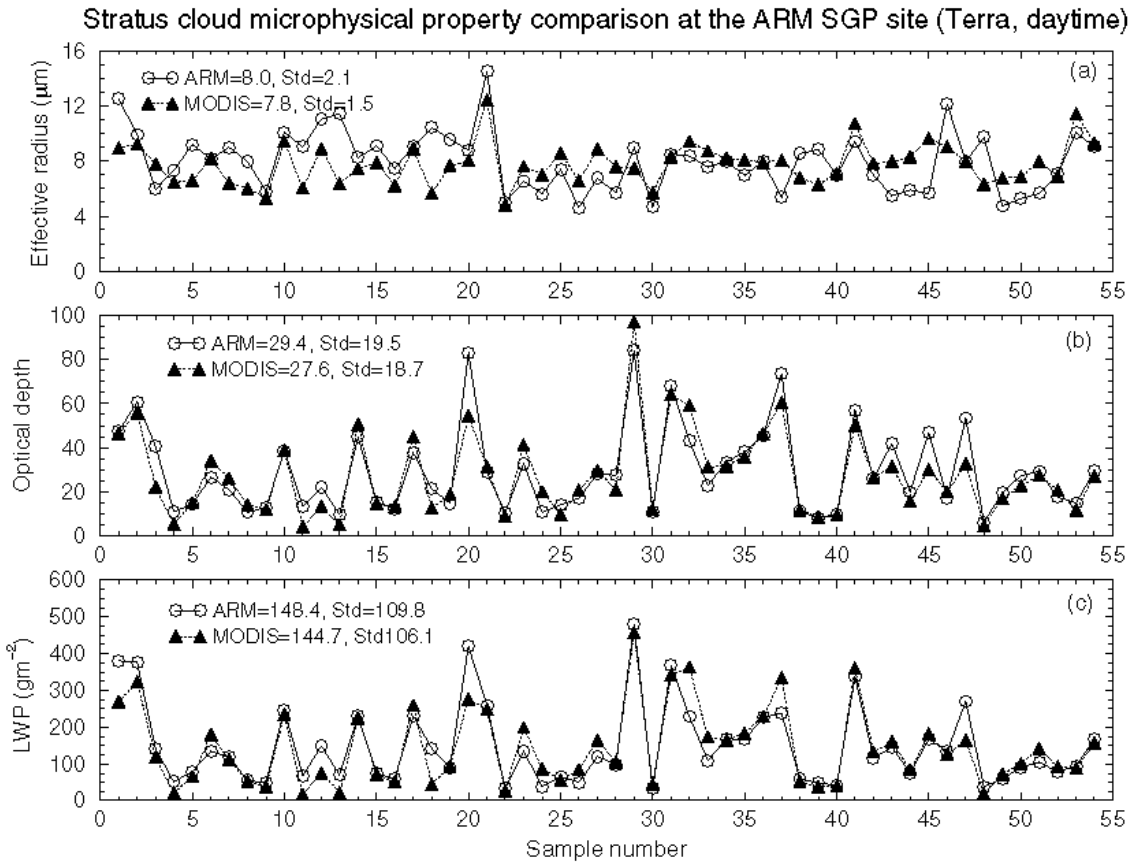

Figure 9. Time series of surface-derived (1-hour average) and matched *Terra* MODIS-derived cloud parameters (30-km x 30-km average), a) cloud-droplet effective radius, b) optical depth, and c) LWP, for daytime single-layer, overcast stratus clouds over the ARM SGP site (sample number is ordered from March 2000 to December 2004).

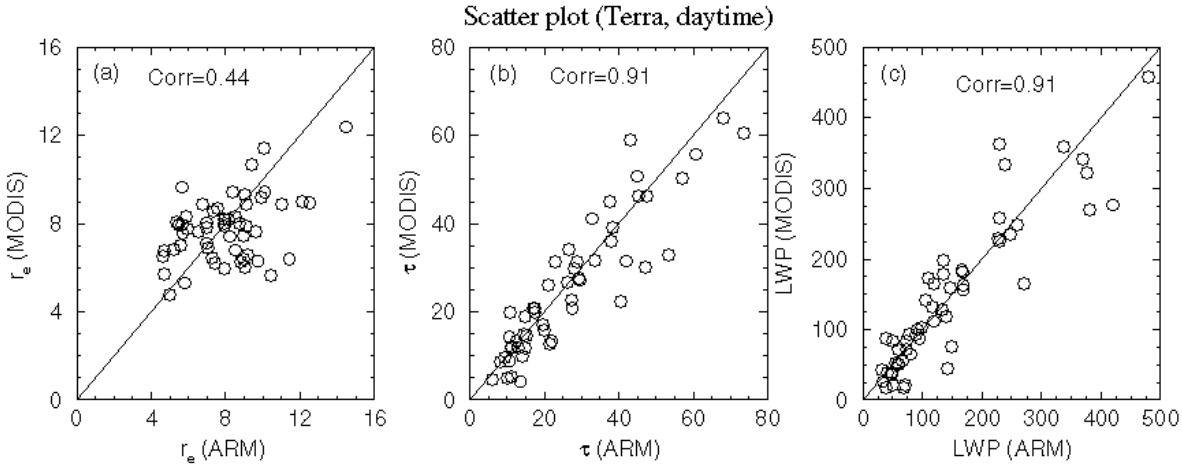

915

916 Figure 10. Scatterplots of data presented in Figure 9.

917

918

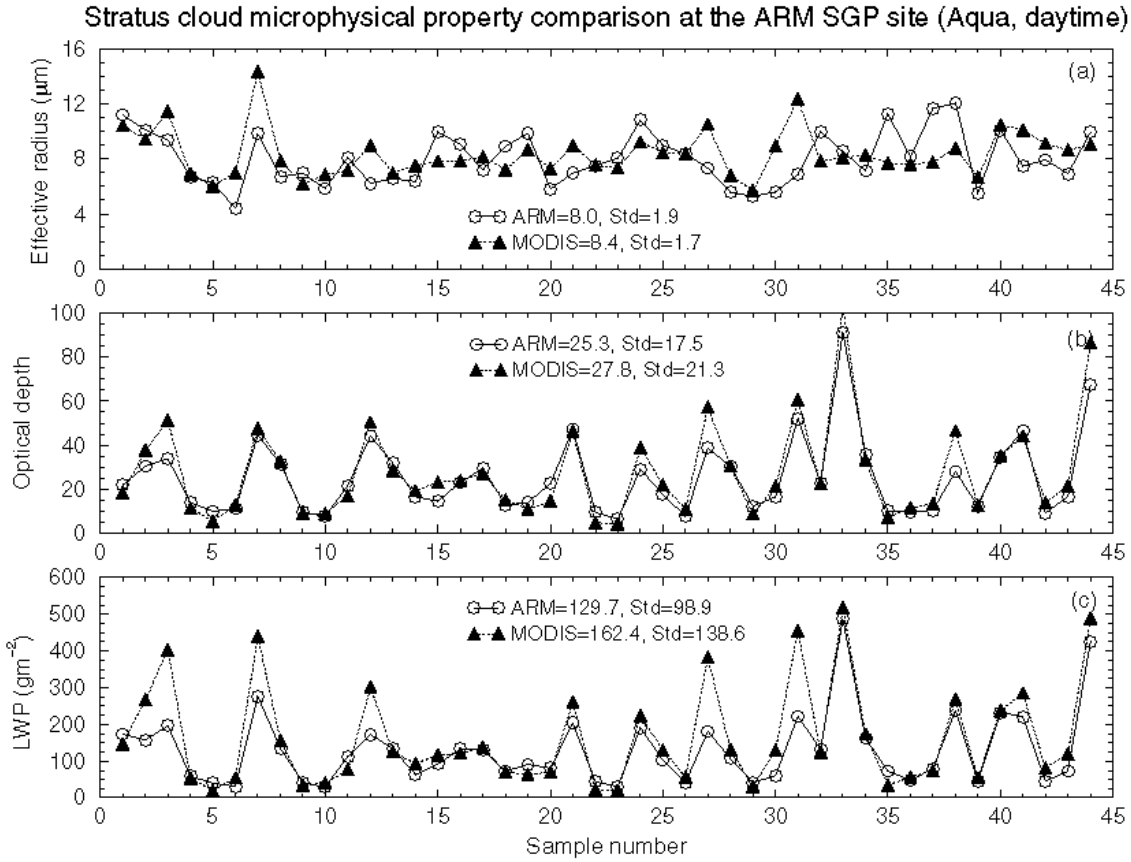

Figure 11. Same as Figure 9, except for *Aqua* (sample number is ordered from July 2002 to December 2004).

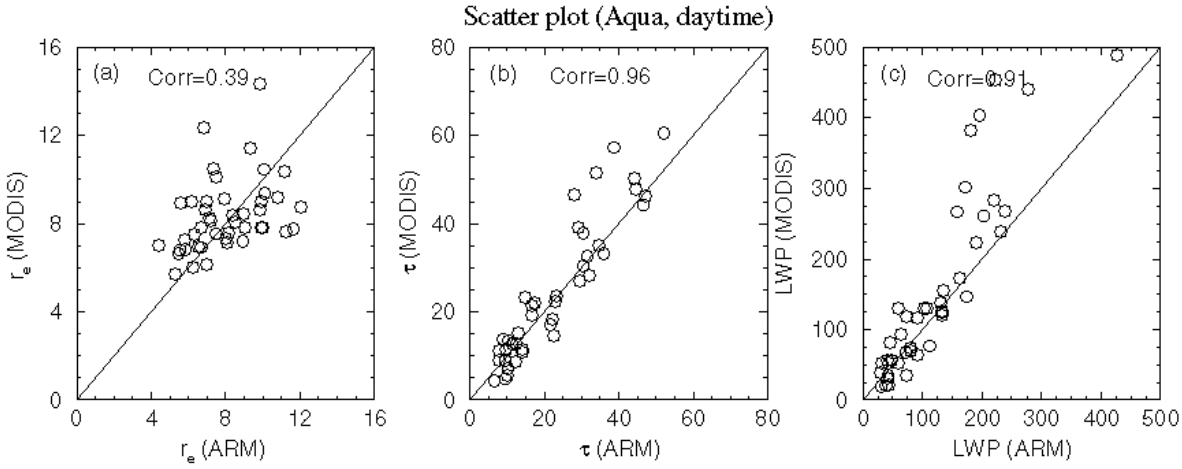

Figure 12. Same as Figure 10, except data from Figure 11 (daytime *Aqua*-surface retrievals) are plotted.

931

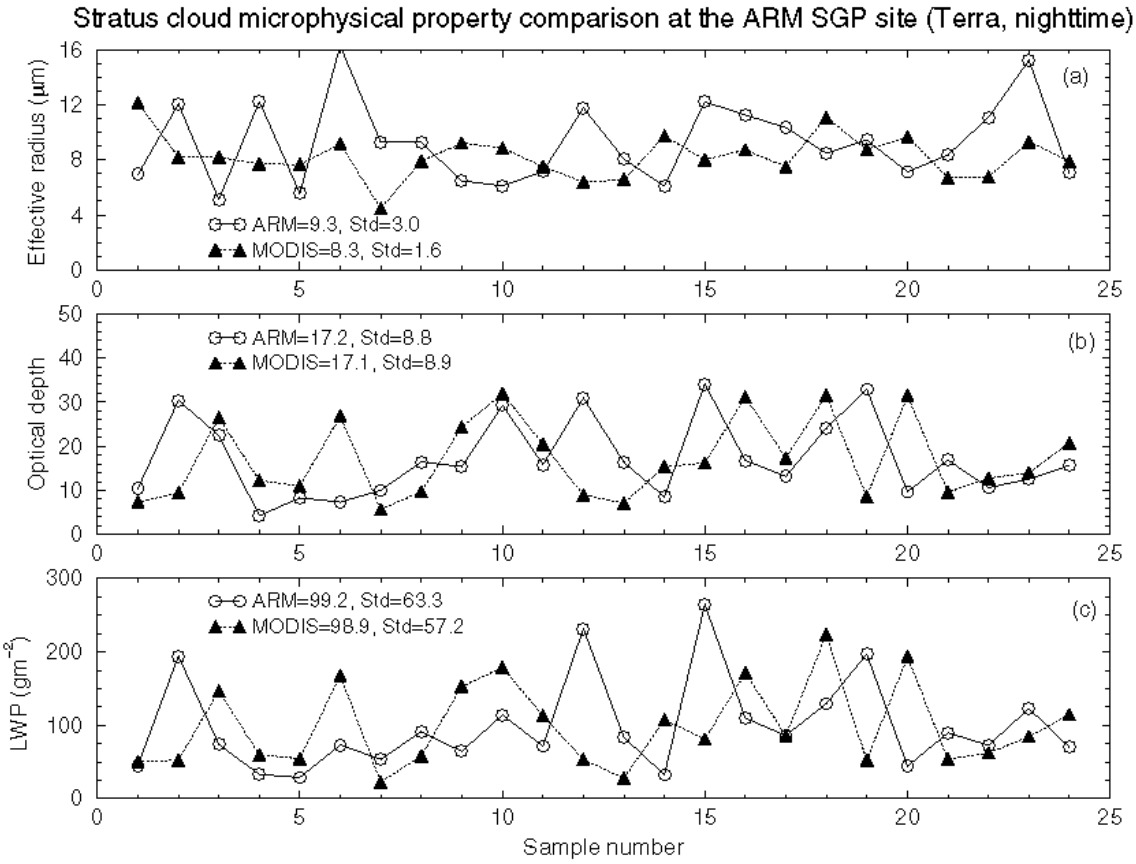

932

933 Figure 13. Same as Fig. 9, except for *Terra* nighttime results.

934

935

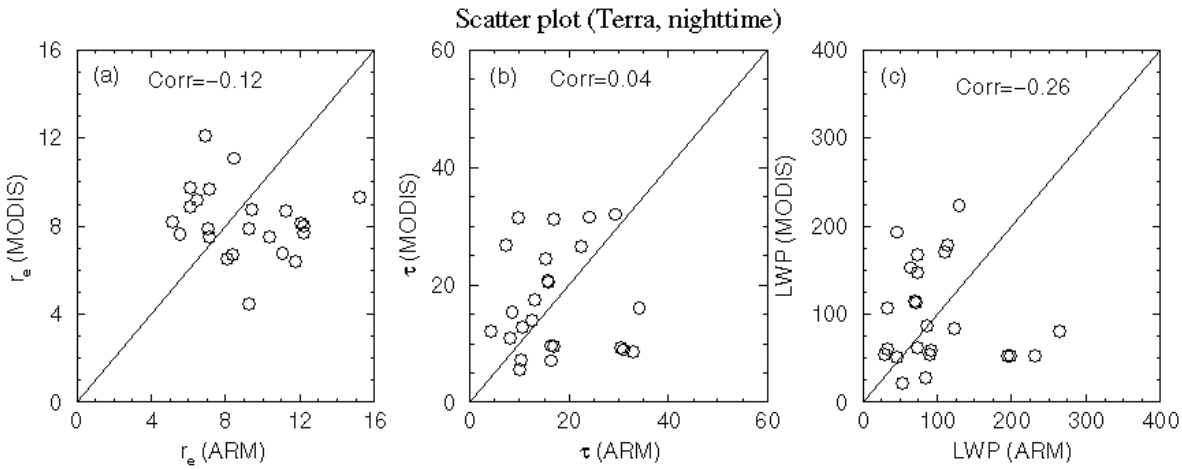

936
937 Figure 14. Same as Figure 10, except results from Figure 13 (nighttime *Terra*-surface retrievals)
938 are plotted.
939

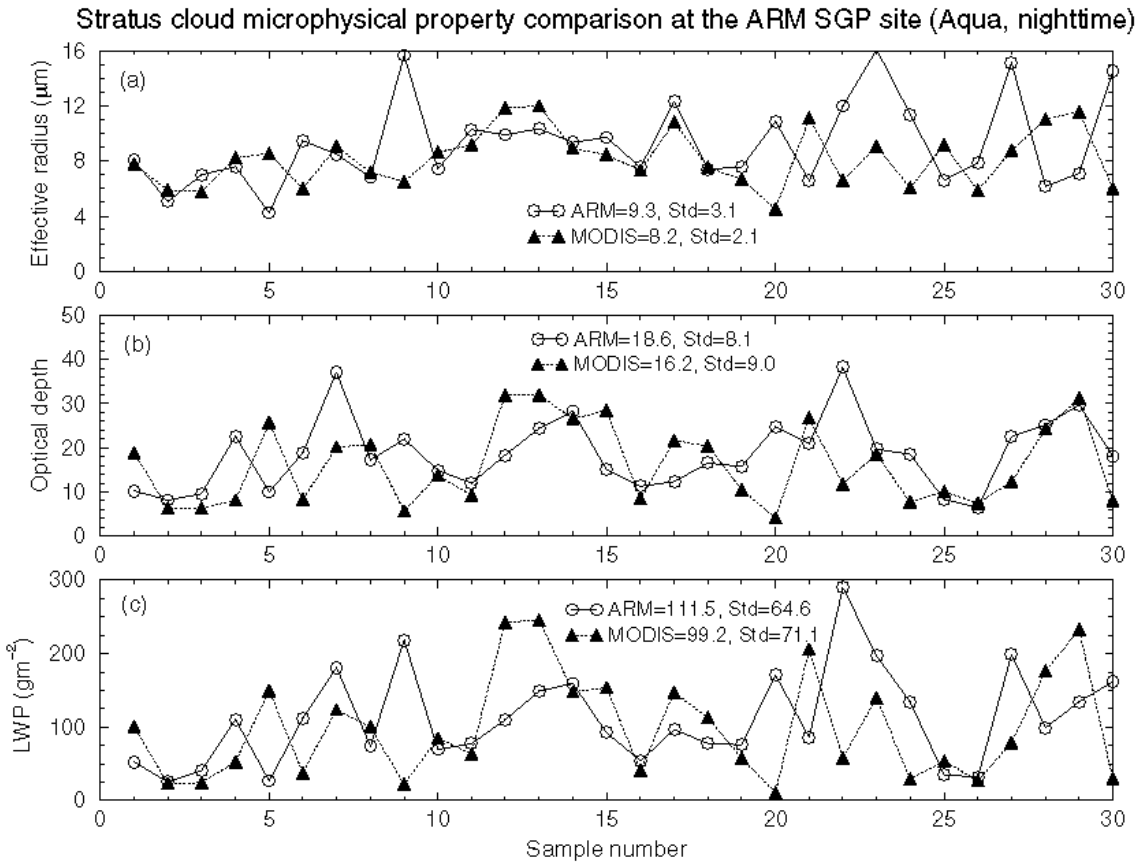

940
941 Figure 15. Same as Fig. 9, except for *Aqua* nighttime results.
942
943

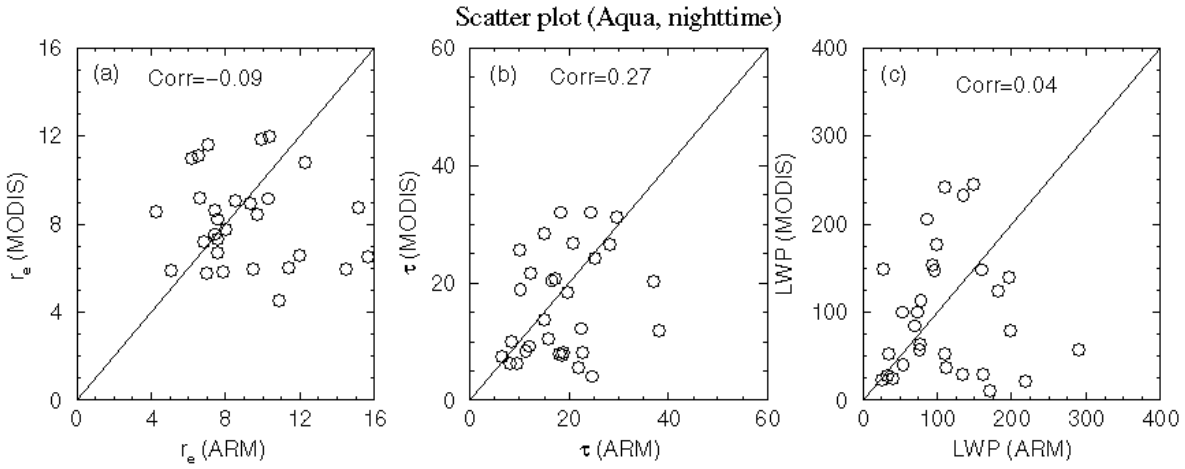

Figure 16. Same as Fig. 10, except for *Aqua* nighttime results.

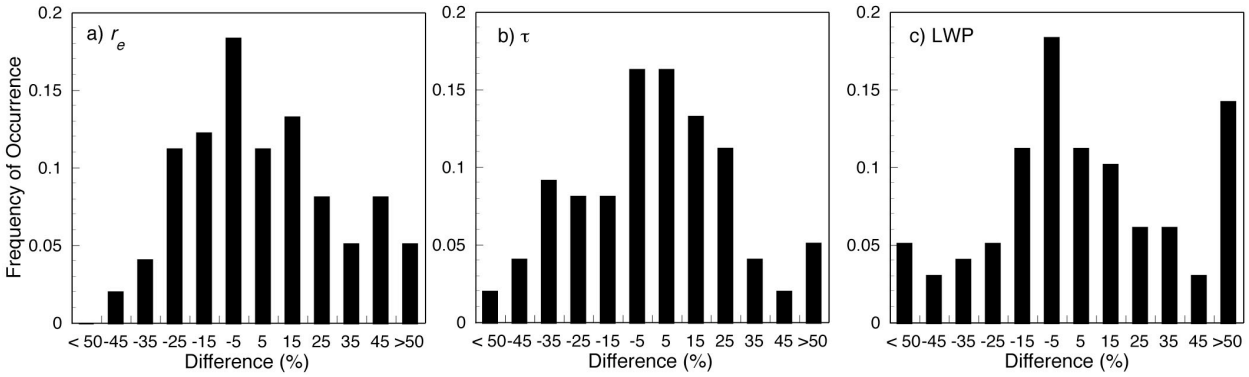

Figure 17. Histograms of daytime cloud property differences between CERES MODIS and surface-based retrievals from data presented in Figures 10 and 12.